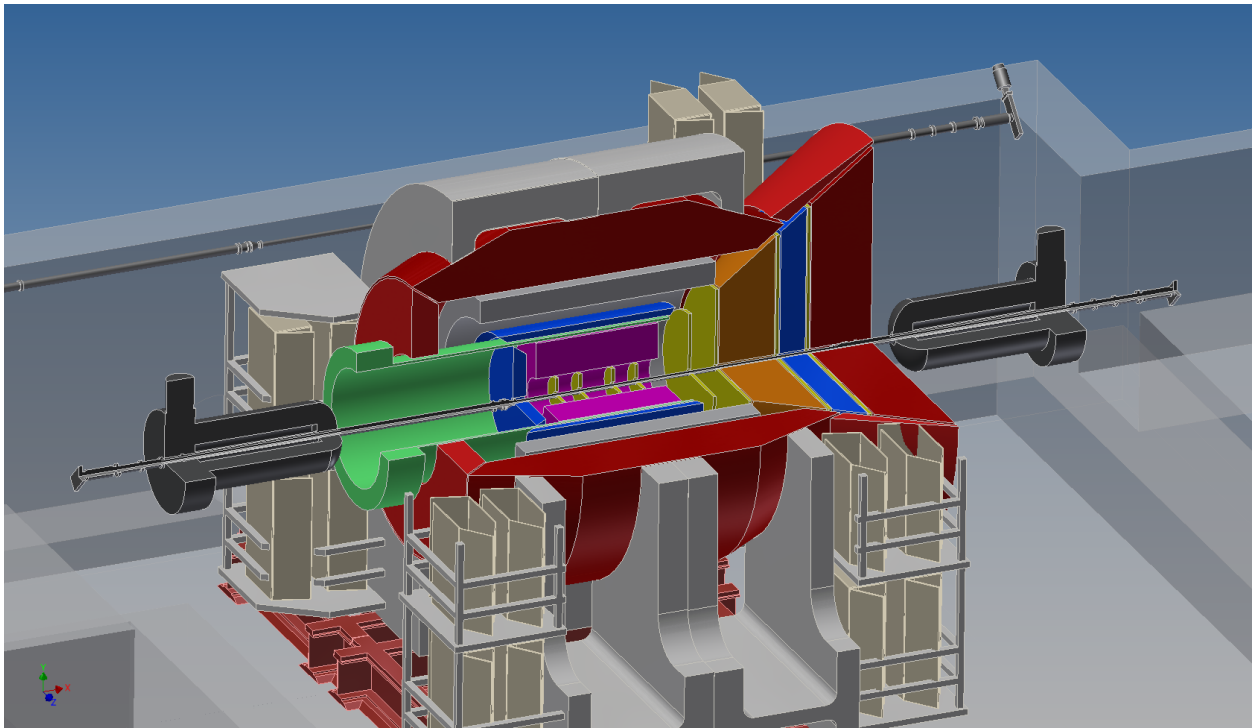# ePH✳ENIX

A Letter of Intent from the PHENIX Collaboration

Version 1.1

October 1, 2013

Executive Summary

The PHENIX collaboration presents here a Letter of Intent detailing a detector for a future Electron Ion Collider (EIC) at Brookhaven National Laboratory. An EIC with a potential turn-on date of 2025 is envisioned with an electron beam energy up to 10 GeV, hadron beam energies up to 255 GeV for protons and 100 GeV/nucleon for gold ions, and design luminosities of 10^{33} cm^{-2}s^{-1} for 10 GeV on 255 GeV $e+p$ collisions. The EIC detector proposed here, referred to as ePHENIX, will have excellent performance for a broad range of exciting EIC physics measurements, providing powerful investigations not currently available that will dramatically advance our understanding of how quantum chromodynamics binds the proton and forms nuclear matter. This Letter of Intent is submitted in response to a charge from the BNL Associate Laboratory Director – shown in Appendix A.

In April 2013, a Major Item of Equipment (MIE) proposal was submitted to the DOE Office of Nuclear Physics for a extensive upgrade to the PHENIX detector. This upgrade, referred to as sPHENIX, consists of new large acceptance electromagnetic and hadronic calorimetry built around the superconducting solenoid recently acquired from the decommissioned BaBar experiment at SLAC. sPHENIX will make key new measurements of probes of the strongly coupled quark gluon plasma (sQGP) and allow for fundamental tests of our picture of its inner workings [1]. From the beginning, it was realized that the sPHENIX detector design, with its large bore superconducting solenoid, midrapidity calorimetry, open geometry, and coupled with the existing investment in infrastructure in the PHENIX interaction region, provides an excellent foundation for an EIC detector. With this in mind, EIC design considerations for the sPHENIX proposal have been incorporated from the start [2].

A full engineering rendering of the ePHENIX detector — showing how ePHENIX builds upon sPHENIX — is shown in Figure 1. In addition to fully utilizing the sPHENIX superconducting solenoid and barrel calorimetry, ePHENIX adds new detectors in the barrel and electron-going and hadron-going directions. In the electron-going direction a crystal calorimeter is added for electron identification and precision resolution. A compact time projection chamber, augmented by additional forward and backward angle GEM detectors, provides full tracking coverage. In the hadron-going direction, behind the tracking is electromagnetic and hadronic calorimetry. Critical particle identification capabilities are incorporated via a barrel DIRC, and in the hadron-going direction, a gas

RICH and an aerogel RICH.

The sPHENIX upgrade could be ready for physics data taking in 2020 and the ePHENIX additions available for the earliest start of EIC physics in 2025. We document a preliminary cost estimate that includes overhead and 50% contingency. For the additional ePHENIX detectors, the cost totals ∼$80M in equipment and ∼$30M in labor. We note that there are exciting prospects for non-DOE and international support and potentially significant cost reduction options.

The physics case for an EIC is documented in depth in the EIC White Paper [3]. An EIC with 5–10 GeV electron beam energies will enable major scientific advances in at least three main areas: 1) Detailed imaging of the spin and momentum structure of the nucleon; 2) Investigation of the onset of gluon saturation in heavy nuclei; and 3) Study of hadronization in cold nuclear matter. In this document we review each area with a focus on the connection to detector acceptance and performance requirements. We consider each subsystem in sufficient detail to be able to map out the performance using both parametrized and full GEANT4 simulations. We find a broad suite of observables where ePHENIX has excellent capabilities.

The ePHENIX detector capably addresses most all of the physics enabled at this EIC machine. We believe we have struck a strong balance between capabilities and costs for ePHENIX, but there remain clear targets for augmenting those capabilities—for instance, by adding a silicon vertex detector to enable measurements of open charm observables (e.g., F_2^c). In addition, there is a possibility to upgrade eRHIC to higher energy electron beams at a future date, and we believe ePHENIX provides an excellent base upon which an upgraded detector capable of exploiting the physics potential of those collisions could be built. There is also the potential, if one can realize appropriate instrumentation in the hadron-going direction while $p+p$ and $p+A$ collisions are still available in RHIC, to pursue a rich program of forward physics measurements.

The PHENIX collaboration itself has outstanding detector expertise and technical support as a base for the construction of an EIC detector. Nonetheless, we view ePHENIX as a fundamentally new collaboration that would require and welcome the addition of new institutions bringing with them additional detector expertise, physics insights, and scientific leadership.

This document is organized as follows. Chapter 1 illustrates the wide spectrum of EIC physics that can be addressed. Chapter 2 describes the detector requirements that follow from that physics and which drive the ePHENIX design. Chapter 3 details the ePHENIX detector concept and shows its performance for key measurements. Chapter 4 details a preliminary cost estimate for the ePHENIX detector. Finally, Chapter 5 describes the way in which the PHENIX collaboration will evolve and grow into a new collaboration to be able to build, operate, and exploit the full physics potential of ePHENIX.
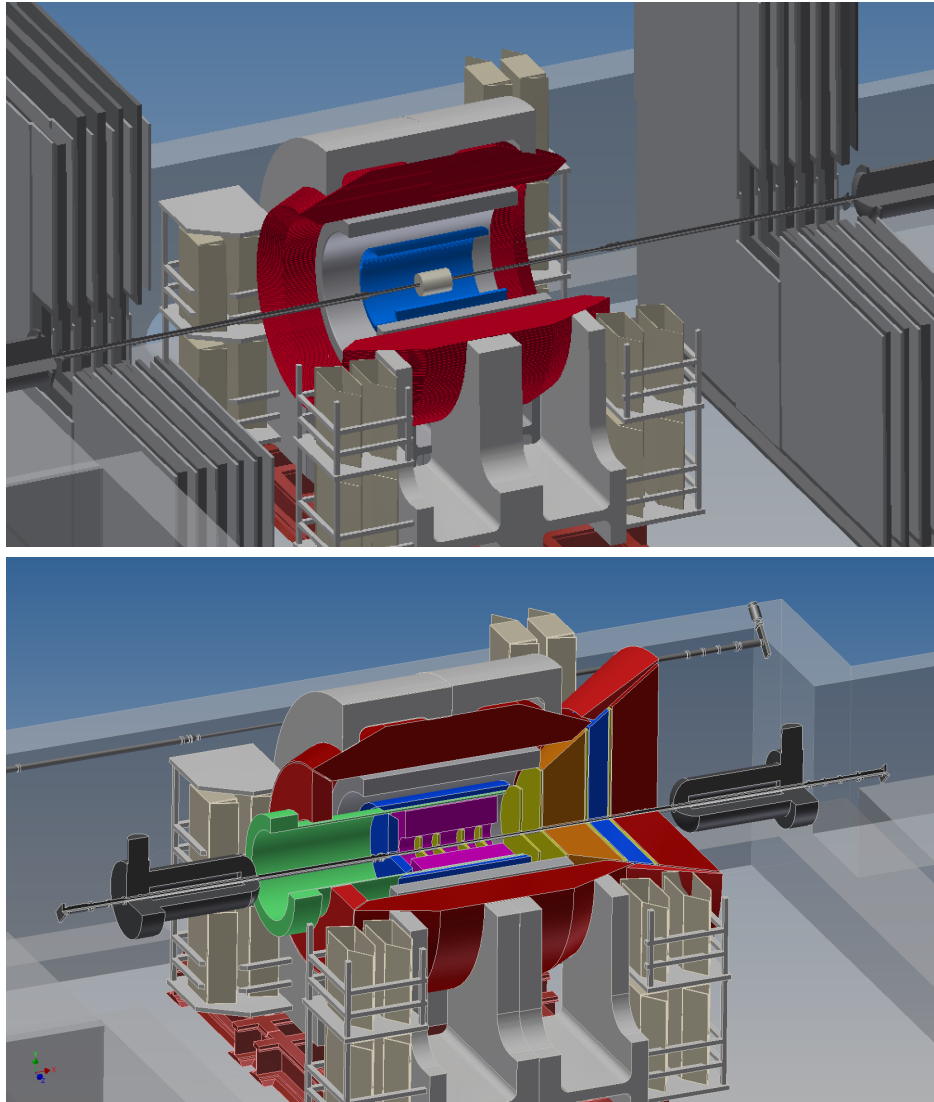
Figure 1: The evolution of the sPHENIX detector, with its focus on jets and hard probes in heavy-ion collisions, into ePHENIX, with additional capabilities supporting its focus on $e+p$ and $e+$A collisions. (top) The sPHENIX detector in the existing PHENIX experimental hall. (bottom) The ePHENIX detector, in the same hall, showing the reuse of the superconducting solenoid and the electromagnetic and hadronic calorimeter system. The eRHIC focusing quadrupoles, each located 4.5 m from the interaction point, and the height of the beam pipe above the concrete floor, set the dominant physical constraints on the allowable dimensions of ePHENIX.

iv

Contents

Chapter 1

Physics at an Electron-Ion Collider

The 2007 Nuclear Physics Long Range Plan [4] states that the Electron-Ion Collider (EIC) embodies "the vision for reaching the next QCD frontier." In this Chapter we review the primary physics goals as detailed in the EIC White Paper [3] and the broad physics program that can be carried out with the ePHENIX detector.

1.1   Fundamental questions addressed by the EIC

The EIC is designed to address several important question that are described in detail in the recent EIC White Paper [3]. Quoting from the White Paper, these questions are reproduced here:

- **How are the sea quarks and gluons, and their spins, distributed in space and momentum inside the nucleon?** How are these quark and gluon distributions correlated with overall nucleon properties, such as spin direction? What is the role of the orbital motion of sea quarks and gluons in building the nucleon spin?

- **Where does the saturation of gluon densities set in?** Is there a simple boundary that separates this region from that of more dilute quark-gluon matter? If so, how do the distributions of quarks and gluons change as one crosses the boundary? Does this saturation produce matter of universal properties in the nucleon and all nuclei viewed at nearly the speed of light?

- **How does the nuclear environment affect the distribution of quarks and gluons and their interactions in nuclei?** How does the transverse spatial distribution of gluons compare to that in the nucleon? How does nuclear matter respond to a fast moving color charge passing through it? What drives the time scale for color neutralization and eventual hadronization?

The White Paper describes in detail the "golden" measurements in inclusive Deep Inelastic Scattering (DIS), Semi-Inclusive DIS (SIDIS), and exclusive scattering at a future $e+p$ and $e+A$ collider which will address the above questions employing a perfect detector.

1.2   eRHIC: realizing the Electron-Ion Collider

The accelerator requirements for an EIC that can answer the questions listed above are spelled out in the EIC White Paper [3]. Two possible designs are presented based on current facilities: (1) the eRHIC design, which adds a Energy Recovery LINAC to the existing RHIC complex at Brookhaven National Laboratory (BNL) which can accelerate polarized protons up to 250 GeV and ions such as gold up to 100 GeV/nucleon, and (2) the ELectron-Ion Collider (ELIC) design, which uses the 12 GeV Upgrade of CEBAF at Jefferson Laboratory with a new electron and ion collider complex.

As per the charge from the Brookhaven National Laboratory Associate Lab Director, we consider the following eRHIC design parameters:

- A polarized electron beam with energy up to 10 GeV and polarization of 70%,

- A polarized proton beam with energy up to 250 GeV and polarization of 70%,

- An ion beam which can run a range of nuclei from deuteron to gold and uranium with energy up to 100 GeV/nucleon for gold,

- Luminosity with a 10 GeV electron beam of 10^{33} cm^{-2}s^{-1} for $e+p$ with 250 GeV proton beam energy, and 6×10^{32} cm^{-2}s^{-1} for $e+A$ with 100 GeV ion beams.

1.3   Physics deliverables of ePHENIX

The three fundamental and compelling questions in QCD to be addressed by the EIC discussed in Section 1.1 can be broken down in to five golden measurements suggested in the EIC White Paper [3].

The first three relate to using the proton as a laboratory for fundamental QCD studies.

- **The longitudinal spin of the proton:** With the good resolution calorimetry and tracking in ePHENIX, Inclusive DIS measurements in polarized $e+p$ collisions will decisively determine the gluon and quark spin contributions to the proton spin. Further, planned particle identification capabilities will allow ePHENIX to pin down the spin contributions from the different quark flavors.

- **Transverse motion of quarks and gluons in the proton:** With the excellent particle identification capabilities of ePHENIX and the high luminosity of eRHIC, unparalleled SIDIS measurements will be possible, and enable us to explore and understand how the intrinsic motion of partons in the nucleon is correlated with the nucleon or parton spin.

- **Tomographic imaging of the proton:** The large acceptance of ePHENIX for tracking and calorimetry, far forward proton and neutron detector capabilities, the high luminosity of eRHIC and the phase space accessible in a collider geometry enables ePHENIX to significantly extend the kinematic coverage of exclusive measurements such as Deeply Virtual Compton Scattering (DVCS). With these, detailed images of how (sea) quarks and gluons are distributed in the proton will become possible for the first time.

The following two relate to extending these techniques to the heaviest stable nuclei.

- **Hadronization and its modification in nuclear matter:** With ePHENIX PID and the versatility of eRHIC to collide many different ions, measurements of identified hadrons in $e+p$ and $e+$A will allow precise study of how quarks hadronize in vacuum and in nuclear matter.

- **QCD matter at extreme gluon density:** ePHENIX will enable measurements of diffractive and total DIS cross-sections in $e+$A and $e+p$. Since the diffractive cross section is viewed as a double gluon exchange process, the comparison of diffraction to total cross section in $e+$A and $e+p$ is a very sensitive indicator of the gluon saturation region. ePHENIX would be an ideal detector to explore and study this with high precision.

Below we discuss each of these points in more detail and with specific details on the ePHENIX capabilities.

1.3.1   The proton as a laboratory for QCD

Deep Inelastic Scattering experiments over the last several decades have greatly enhanced our understanding of the proton substructure. Measurements with colliding beams at H1 and ZEUS at HERA have mapped out the momentum distributions of quarks and gluons, and shown that the gluons carry roughly half of the proton momentum. Fixed target experiments, with polarized nucleons and leptons at SLAC, CERN, DESY and JLab have revealed new surprises about proton structure, finding that only a small fraction of the proton spin comes from the quark spin and that there is significant correlation between the intrinsic motion of quarks and the nucleon spin. Measurements at both fixed target and colliders have started to image the proton through exclusive measurements.
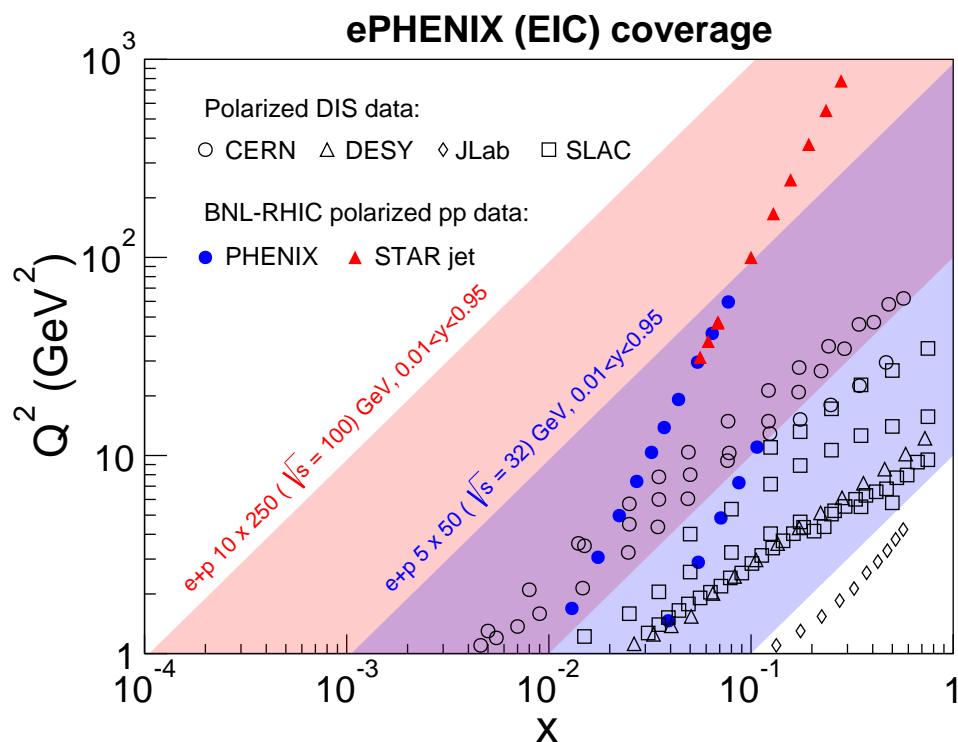
ePHENIX (EIC) coverage

Figure 1.1: Kinematic coverage of ePHENIX for two beam energy configurations, 10×250 GeV and 5×50 GeV, which show the range of eRHIC capabilities. Also shown are data from current polarized fixed target DIS experiments and RHIC $p+p$ collisions.

eRHIC will greatly enhance the kinematic coverage for DIS with polarized beams, as shown in Figure 1.1. With the capabilities of ePHENIX, we will significantly extend our understanding of the proton. The gluon and flavor dependent sea quark spin contributions to the proton spin will be determined, as will the possible orbital angular momentum contributions. The spatial and momentum distributions of (sea) quarks and gluons can be mapped, giving a multidimensional description of the proton.

Longitudinal spin of the proton

The puzzle of the proton spin, to which the quark spin only contributes roughly a third, has spurred two decades of study. Measurements from fixed target polarized DIS have determined the quark contribution, but are less sensitive to the gluon due to the small kinematic coverage. Current RHIC measurements indicate that the gluon spin contribution may be comparable or even larger than the quark spin contribution, but due to the limited coverage at low longitudinal momentum fraction, x, large uncertainty remains, as is shown in Figure 1.2 (yellow band).

Determining the gluon longitudinal spin contribution is a primary goal of the EIC and of ePHENIX, and will be possible due to the large reach in x and four-momentum transfer squared, Q^2. Figure 1.2 shows the expected impact from ePHENIX measurements of inclusive DIS on the uncertainty of the gluon helicity distribution as a function of x.

With the ePHENIX particle identification (PID) detectors, measurements of pions and kaons will greatly improve on the determination of the sea quark longitudinal spin distribution as well, including that of the strange quark, Δs, which has been of particular interest in the last few decades, because of the contradictory results obtained from different data. Current global analyses use hyperon beta decay to constrain Δs, which indicates a negative value for the full integral over x. Fixed target SIDIS measurements of kaon asymmetries, which directly probe Δs, though at low values of Q^2 and in a limited x range, find a positive contribution for $x > 0.01$. eRHIC provides data over a wide x and Q^2 range. Further, ePHENIX will provide excellent particle ID capability to identify kaons and allow direct measurements of strangeness spin contribution to the nucleon down to $\sim 2 \times 10^{-4}$.

Transverse motion of quarks and gluons in the proton

Large transverse spin asymmetries measured in fixed target SIDIS in the past decade have spurred significant theoretical work. These asymmetries relate to the transversity distribution, the correlation between the transverse spin of the proton and a transversely polarized quark in it, and Transverse Momentum Distributions (TMDs), such as the Sivers or Boer-Mulders distributions, which describe correlations between either the proton or quark spin and the quark intrinsic motion, specifically the transverse momentum of the quark. With measurements of identified pions and kaons, these asymmetries give a 2+1 dimensional description of the spin and momentum distributions of different quark flavors in the proton, such as is shown in Figure 1.3.

Current measurements, however, are only able to probe a small region in x and Q^2, limiting the description to the valence quark region. Understanding of how the sea quarks and gluons contribute requires a larger kinematic range, such as provided at eRHIC. With the PID capabilities of ePHENIX, asymmetry measurements with transversely polarized nucleons and electrons in SIDIS will enable the study of these TMDs over most of this range, significantly expanding our knowledge of the proton structure. The constraint on the Sivers distributions was discussed in the EIC White Paper [3], with the expectations shown in Figure 1.3. For the first time, determination of the Sivers distribution over a wide range in x will be possible, including the low x region where gluons dominate.

The transversity distribution, when coupled with the Collins fragmentation asymmetry, would result in an azimuthal asymmetry in the hadron production. This has been called the Collins effect, and is a measurement that goes to the heart of establishing the transversity distribution in a proton [6]. Measurement over the wide kinematic region would not only allow us to measure transversity, but the wide x-coverage possible at eRHIC would afford the first reliable measurement of the tensor charge of the proton (the integral over x of the
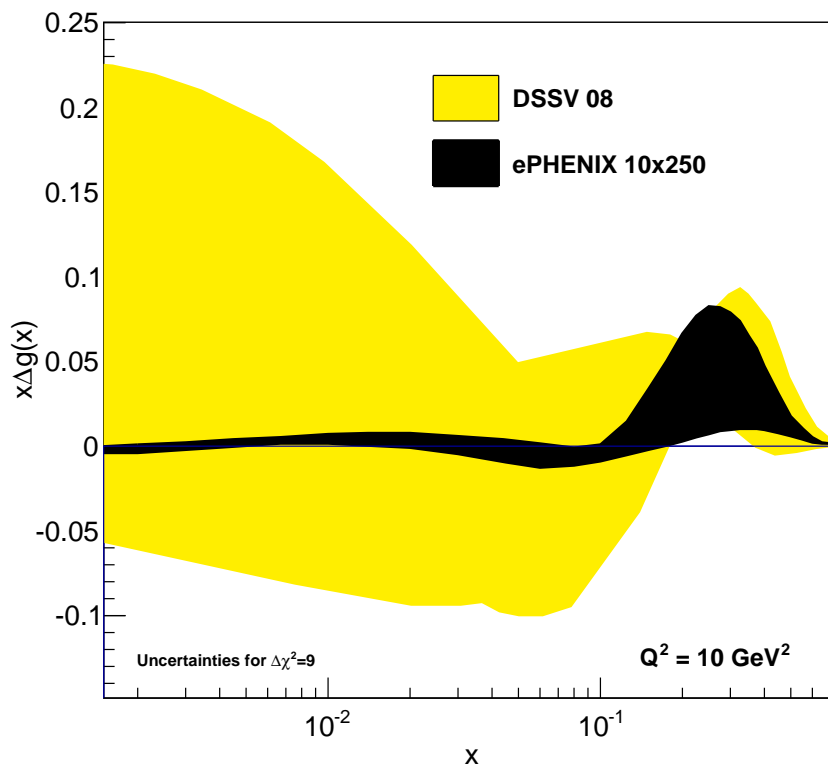
Figure 1.2: The projected reduction in the uncertainty (black) on the gluon longitudinal spin distribution based on simulated PYTHIA events corresponding to an integrated luminosity of 10 fb^{-1} at the 10 GeV $\times$ 250 GeV beam energy configuration. A 1% systematic uncertainty in beam and target polarization is applied. The yellow area shows the uncertainty from current data based on the analysis in Ref. [5].

transversity distribution). No other currently operational or planned facility can do this.

Tomographic imaging of the proton

Hard exclusive processes such as the Deeply Virtual Compton Scattering (DVCS) and Deeply Virtual Vector Meson production (DVVM) involve interactions between the virtual photon and the partons in the proton without breaking the proton, resulting in the production of a real photon in DVCS or a vector meson in DVVM processes. Just as elastic lepton-nucleon scattering gives information on the spatial distribution of the electric charge and magnetization in the nucleon, DVCS and DVVM processes probe the transverse distribution of quarks, anti-quarks and gluons. This information is encoded in generalized parton distributions (GPDs), which quantify the distributions of quarks and gluons in terms of their positions in the transverse plane and longitudinal momentum fraction,
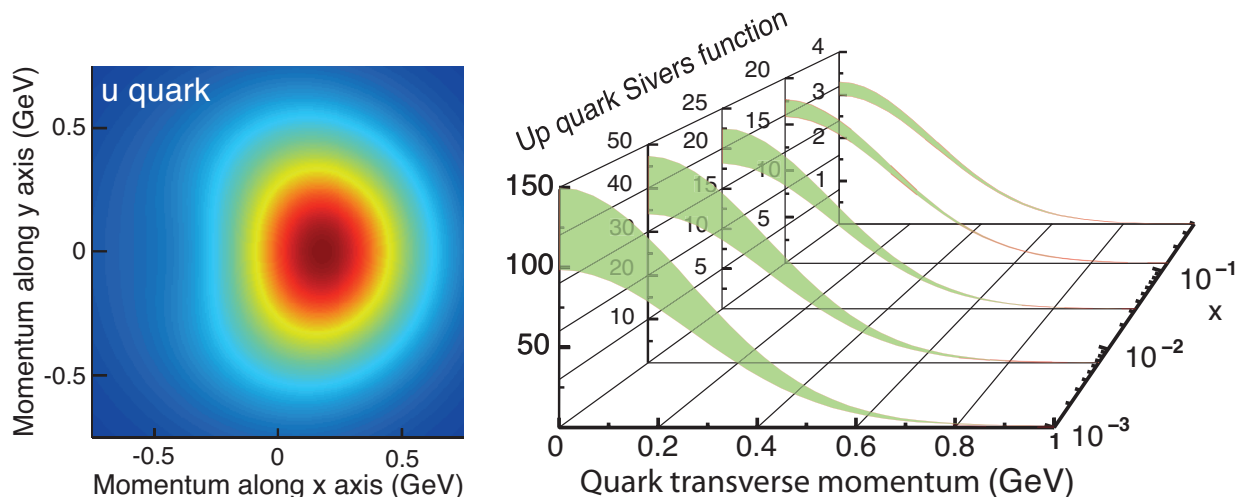
Figure 1.3: [Reproduced from Ref. [3].] (left) The transverse-momentum distribution of an up quark with longitudinal momentum fraction $x = 0.1$ in a transversely polarized proton moving in the z-direction, while polarized in the y-direction. The color code indicates the probability of finding the up quarks. (right) The transverse-momentum profile of the up quark Sivers function at five x values accessible with the kinematics avialable at eRHIC, and corresponding statistical uncertainties.

providing 2+1 dimensional imaging of the nucleon. Measurements with polarized beams enable studies of spin-orbit correlations of quarks and gluons in the nucleon, by correlating the shift in the parton transverse distribution and proton transverse polarization. It is intuitively connected with orbital angular momentum carried by partons in the nucleon and hence of great interest in addressing the nucleon spin puzzle (nucleon spin decomposition) [7].

The existing data on GPDs from fixed target experiments cover only a limited kinematical range of t (the squared momentum transfer to the proton), medium to high x and low Q^2. The t is connected through the Fourier transform with the impact parameter range probed. While data from HERA collider experiments (ZEUS and H1) covered lower x and a wide range in Q^2, they are statistically limited. Furthermore, the HERA proton beams were unpolarized, so ZEUS and H1 were not able to study the proton-spin dependence in these measurements. With its large acceptance, excellent detection capabilities, high luminosity and broad range of energies of the polarized proton/helium beams available at eRHIC, ePHENIX will provide high precision data over a wide range of x, Q^2 and t. The wide range in t possible at eRHIC is of crucial importance, and will be achieved by integrating Roman Pot detectors in the accelerator lattice from the outset. Similar measurements performed with ion beams will allow analogous imaging of nuclei, allowing the first look at the parton distributions inside the nuclei.

The EIC White Paper demonstrates the precision that can be achieved in such a program with Deeply Virtual Compton Scattering (DVCS) and exclusive J/ψ production. The

7

detector requirements for such measurements discussed in the White Paper and what we propose as ePHENIX are similar. For such, we expect ePHENIX will be able to make high impact measurements of GPDs.

1.3.2   Nucleus as a laboratory for QCD

Electron scattering interactions from nuclei allow key tests of the modification of parton distribution functions in nuclei of various sizes. The EIC has the unprecedented energy reach to probe deep into the low-x quark and gluon region where there are predictions of significant non-linear evolution effects and possibly the realization of a universal state of the QCD vacuum at high gluon density. In addition, rather than looking at the modified number of deep inelastic scatterings, one can study via SIDIS the changes in the process of a highly virtual struck quark to color neutralize and eventually hadronize when in the presence of a nuclear medium.

Hadronization and its modification in nuclear matter

Deep inelastic scattering with heavy nuclear targets provides an effective stop watch and meter stick with which one can measure the color neutralization and hadronization times, and understand important details of partonic interactions with the nucleus. By varying the size of the nuclear target (at eRHIC all the way up to uranium) and changing key DIS parameters $(Q^2, \nu, z, p_T^2, \phi)$ one can calibrate this watch and meter stick. Figure 1.4 shows the kinematic reach for 5 GeV electrons scattering from 100 GeV/nucleon heavy nuclei in terms of the initial virtuality Q^2 and the energy of the struck quark in the nuclear rest frame ν. Earlier experiments with fixed targets have measured very interesting modifications in apparent fragmentation functions, and yet those results are limited to small values of Q^2 and ν. In the case of the published HERMES results [8] in Fig. 1.4, one observes a dramatic decrease in the number of high-z hadrons (those with a large fraction of the struck quark momentum) in scattering from nuclear targets. There are many possible explanations of the experimental results, including parton energy loss due to multiple scattering in the nucleus and induced gluon radiation — a similar mechanism has been used to explain the "jet quenching" phenomena discovered in heavy ion collisions at RHIC. Other theoretical frameworks predict a strong correlation between a short color neutralization timescale and high-z resulting processes. An excellent review of the various theoretical approaches is given in Ref. [9]. Figure 1.4 also shows the expected statistical precision with the ePHENIX PID capabilities over the full ν range in one Q^2 bin.

If the struck quark remains an undressed color charge while it traverses the nucleus, one might expect that the ratio of final state hadrons (π^+, K^+, p and their anti-particles) would show the same degree of nuclear modification. Shown in the right panel of Figure 1.4 are the double ratios of modifications R_{Xe} with a xenon target for antiprotons to protons and K^- to K^+. It is notable that there is a larger suppression for the hadrons with a
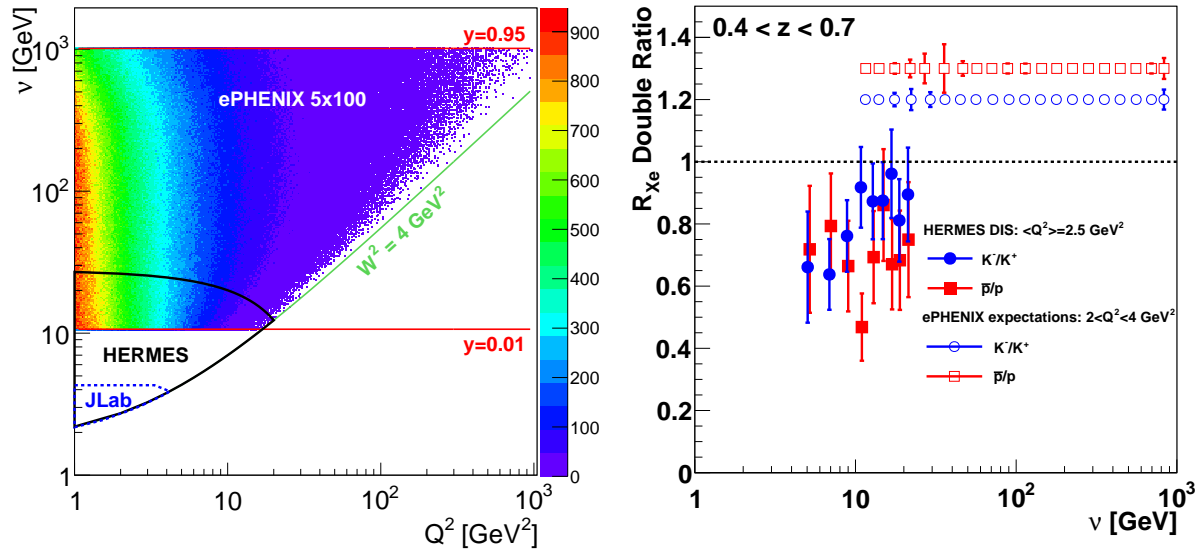
Figure 1.4: (left) Shown is the very large virtuality Q^2 and ν coverage for ePHENIX (EIC) measurements with collisions of 5 GeV electrons on 100 GeV/nucleon heavy nuclei. The z-axis color scale shows the relative distribution of events from the PYTHIA event generator. Also shown are the kinematic reach for the CLAS experiment at JLab [10] and for the HERMES results [8]. (right) Experimental data from HERMES [8] on the modified fragmentation from xenon targets (R_{Xe}) in the range $0.4 < z < 0.7$ and with average $\langle Q^2 \rangle = 2.5$ GeV^2. The filled points are the double ratio for antiprotons relative to protons (red) and for K^- relative to K^+ (blue). ePHENIX will measure with precision the modified fragmentation distribution with excellent π, K, p particle identification over a very broad range of Q^2 and ν. The open symbols show the expected statistical precision for ePHENIX with its particle identification capabilities for one bin in Q^2, $2 < Q^2 < 4$ GeV^2 based on 2 fb^{-1} at the 5 GeV $\times$ 100 GeV beam energy configuration.

larger cross section with nucleons (e.g. $\sigma_{\bar{p}+N} > \sigma_{p+N}$ and $\sigma_{K^-+N} > \sigma_{K^++N}$). If this is due to hadronization occurring within the nucleus, then inelastic collisions can result in the differential attenuation. How does this attenuation vary with the energy of the struck quark? The EIC realization has the enormous reach in the energy of the struck quark ν at fixed Q^2 to measure the full evolution with high statistics. As demonstrated in this document, ePHENIX will have excellent π, K, p particle identification to make exactly this measurement with high statistics. In addition, one can vary the virtuality which is also expected to play a significant role in the length scale probed in the nucleus and thus rate of initial radiation.

Tests with charm mesons via displaced vertex measurements are not in the initial suite of ePHENIX capabilities, and could be added with a later inner thin silicon detector. Measurements of the interactions of charm quarks with the nucleus would be quite interesting in the context of suppressed radiation due to the "dead-cone" effect. However, the relation to kinematic variables z and ν may depend on the balance of DIS events from intrinsic charm as opposed to photon-gluon fusion reactions resulting in $c\bar{c}$ pair

production.

QCD matter at extreme gluon density

A key goal of any future EIC is to explore the gluonic matter at low x, where it is anticipated that the density of gluons will saturate as the rate of gluon recombination balances that of gluon splitting. In fact, there are well known modifications to the quark distribution functions in nuclei that have significant x dependence: high x Fermi motion effects, then the EMC suppression, anti-shadowing enhancement, and finally nuclear shadowing at the lowest x. The ePHENIX detector, combined with the large kinematic reach of an $e+A$ collider, is in an excellent position to map this physics out in the gluon sector.
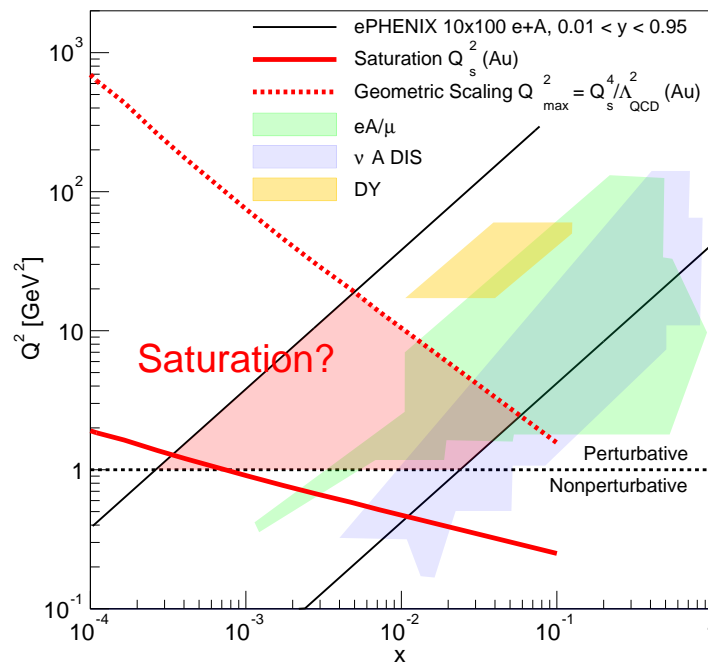
Figure 1.5: Shown is the coverage in x and Q^2 for the EIC and the ePHENIX detector for 10 GeV electrons on 100 GeV/nucleon heavy nuclei. The two black lines indicate the kinematic coverage with selections on the inelasticity $0.01 < y < 0.95$ (which might be slightly reduced depending on the final electron purity at low momentum). Also shown are the kinematic coverage by previous experiments in $e+A$ and $\nu+A$ DIS and also Drell-Yan measurements. The red solid line is an estimate of the x dependence for the saturation scale Q_s^2. The region where this universal saturated matter dictates the physics is estimated to extend over the geometric scaling region up to $Q_{max}^2 = Q_s^4/\Lambda_{QCD}^2$ shown by the red dashed line [11].

The lowest x regime with saturated gluon densities is unique to QCD, as gluons carry the QCD charge, "color", and so interact with themselves. In order to explore this saturation region, one must probe nuclear matter at high center-of-mass energy, so as to reach as low

in x as possible while still in the perturbative QCD regime (i.e., $Q^2 > 1\,\text{GeV}^2$). Generally, a saturation scale, Q_s, is defined to indicate the onset of saturation (where the gluon splitting and recombination balance each other), with Q_s falling as x increases. In reality the point at which recombination starts to balance the gluon splitting is a range in x and Q^2 and so making measurements over a wide range in x and Q^2 is necessary to fully understand these effects.

eRHIC will have a significantly lower center-of-mass energy than HERA, and so cannot improve upon the minimum x probed with measurements in $e+p$. However, eRHIC will also be capable of accelerating heavy ions in $e+$A collisions. As the x probed is related to the resolution of the probe, collisions at the same Q^2 can resolve significantly lower x due to the larger extent of the nucleus: the partons in the highly accelerated nucleus are probed coherently. This effectively reduces the x probed in $e+$A collisions by a factor of $A^{\frac{1}{3}}$, with A the atomic weight, as this is proportional to the size of the nucleus. At the energies planned for eRHIC, based on measurements in $p(d)+$A, one expects saturation effects in inclusive DIS in $e+$A.

Figure 1.5 shows the x and Q^2 coverage of ePHENIX for the 10 GeV $\times$ 100 GeV/nucleon configuration compared with the current fixed target data. Two red lines are drawn, one (solid) showing expectations of Q_s^2 in $e+$Au and the other (dashed) showing the expected turn on of geometric scaling, which relates to the saturation scale by $Q_{max}^2 = Q_s^4/\Lambda_{QCD}^2$. The shaded red region is where ePHENIX can search for saturation effects.

As described in the EIC White Paper [3], it can be even more effective to explore this region of dense gluonic matter with diffractive physics, where at least two gluons are exchanged in the interaction. Therefore, a primary measurement to probe saturation effects at eRHIC will be comparing the diffractive-to-total cross-section from $e+p$ and $e+$A. The ratio of these cross-sections will directly relate to the size of any saturation effects. Figure 1.6, taken from the EIC white paper [3], shows the prediction of one saturation model for this cross-section ratio with and without saturation, indicating large possible effects. Note that the statistical and systematic uncertainties in this plot are scaled up by a factor of 10 in order to be visible. This measurement relies on measuring events with a large rapidity gap, which is the signature of diffractive events due to the fact that the hadron remains intact after the scattering (though in the case of ions, the nucleus may still break up). The ePHENIX detector will have wide calorimetric coverage, and so will be able to make a measurement of the ratio of diffractive-to-total cross-sections with comparable precision as shown in Figure 1.6.

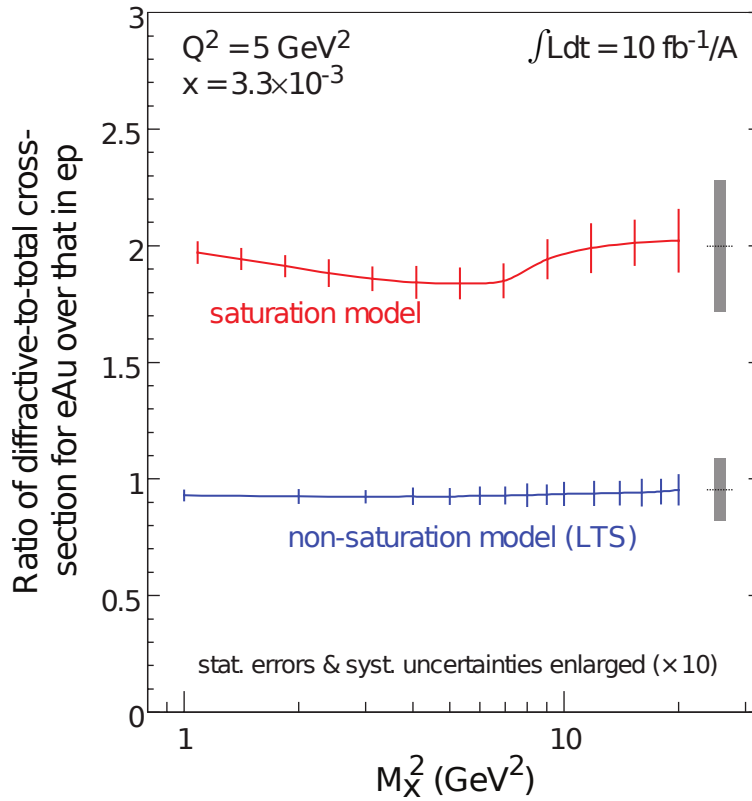**Figure 1.6:** [Reproduced from Ref. [3].] Ratio of diffractive-to-total cross-section for $e+$Au normalized to $e+p$ plotted as a function of the squared mass of the hadronic final state, M_X^2. The expected uncertainties for 10 fb^{-1} are scaled by a factor of 10 to be visible. The ePHENIX detector will have similar capabilities as was assumed for this plot, and will achieve similar precision.

Chapter 2

Detector Requirements

The detector requirements for Deep Inelastic Scattering measurements are well established by previous DIS experiments (H1, ZEUS, HERMES, COMPASS, etc.) and by EIC group studies [3, 9]. Table 2.1 summarizes these basic requirements and how ePHENIX would meet them. After a brief overview of the relevant kinematic variables, detailed studies are presented in this chapter.

The suggested ePHENIX detector configuration is shown in Figure 1. It is built around the sPHENIX detector, which is a superconducting solenoid and electromagnetic and hadronic calorimeter in the central region ($-1 < \eta < 1$ for pseudorapidity η). This proposal would add to that detector the following detector subsystems:

electron-going direction ($-4 < \eta < -1$**):** High resolution Crystal EMCal with GEM tracking.

Barrel ($-1 < \eta < 1$**):** Compact-TPC for low mass tracking and PID for momentum $p < 4$ GeV/c with DIRC

hadron-going direction ($1 < \eta < 4$**):** Hadronic and Electromagentic calorimeters, GEM trackers, and Aerogel-based ($1 < \eta < 2$) and gas-based RICH for PID up to momentum $p \sim 50$ GeV.

Far-Forward in hadron-going direction: Roman Pots and Zero-Degree Calorimeter.

2.1   Kinematics

In DIS, a lepton is scattered off a target hadron via the exchange of a virtual boson, which for electron beam energy $E_e < 10$ GeV can always be taken as a virtual photon. Defining

Table 2.1: Detector requirements

Detector requirements	Detector solution
Electron-ID: High purity (99%) identification of the scattered lepton over hadron and photon background *Important for electron-going direction and barrel acceptance*	Electromagnetic Calorimetry and charged particle tracking Minimum material budget before EMCal Good energy and tracking resolution for E/p matching
Resolution in x and Q^2: Excellent momentum and angle resolution of the scattered lepton to provide high survival probability (80%) in each (x,Q^2) bin (important for unfolding) *Important for electron-going direction and barrel acceptance*	High resolution EMCal and tracking in electron-going direction Good (tracking) momentum resolution for $E'_e < 10\,\text{GeV}$ in barrel Good (EMCal) energy resolution for $E'_e > 10\,\text{GeV}$ in barrel
Hadron identification: $> 90\%$ efficiency and $> 95\%$ purity	In barrel acceptance: DIRC for $p_h < 4\,\text{GeV/c}$ In hadron-going direction: Aerogel for lower momentum and gas RICH for higher momentum
Wide acceptance for leptons and photons in DVCS: Ability to measure DVCS lepton and photon within $-4 < \eta < 4$	EMCal and tracking with good resolution over for lepton and photon measurements covering $-4 < \eta < 4$
Electron/Photon separation: Separate DVCS photon and electron in electron-going direction	High granularity EMCal in electron-going direction
Measurement of scattered proton in exclusive processes	Roman pots in hadron-going direction
"Rapidity gap" measurement capabilities: Measure particles in $-2 < \eta < 4$ for diffractive event identification	Hadronic calorimetry covering $-1 < \eta < 5$, and EMCal covering $-4 < \eta < 4$
Forward Zero-Degree calorimetry: Measure neutrons from nucleus breakup in diffractive $e+$A events	Zero-Degree calorimeter in hadron-going direction planned, in coordination with CAD

the four-momenta of the incoming and scattered electron and the incoming proton as k, k' and p respectively, we can define the following Lorentz invariant quantities:

$$s \equiv (k+p)^2 = 4 E_e E_p \tag{2.1}$$

$$Q^2 \equiv -q^2 = -(k-k')^2 = 2 E_e E_e' \left(1 - cos\theta\right) \tag{2.2}$$

$$y \equiv \frac{p \cdot q}{k \cdot p} = 1 - \frac{E_e'}{E_e} + \frac{Q^2}{4 E_e^2} \tag{2.3}$$

$$x \equiv \frac{Q^2}{2 p \cdot q} = \frac{Q^2}{ys} \tag{2.4}$$

$$\nu \equiv \frac{p \cdot q}{M} = \frac{Q^2}{2Mx} \tag{2.5}$$

where s is the center-of-mass energy squared, q is the 4-momentum transferred from scattered electron and Q^2 is the virtuality of the photon which gives the resolution scale of the scattering, y is the inelasticity of the scattering and x is Bjorken x, the fractional momentum carried by the struck parton. Here, we have also written these in the lab frame in terms of the measured scattering angle, θ and the energies of the proton and incoming and scattered electron, E_p, E_e and E_e', respectively, under the approximation that the electron and proton mass are small compared to the beam energies.

For inclusive DIS, where only the kinematics of the scattered lepton are measured, Eq. 2.1–2.5 fully describe the event. For SIDIS, in which a final state hadron is also measured, additional variables are needed. The fraction of the scattered parton's momentum carried by the hadron is defined as

$$z \equiv \frac{p_h \cdot p}{q \cdot p} \tag{2.6}$$

where p_h is the four-momentum of the measured hadron. Further, we can define $p_{h\perp}$ as the transverse momentum of the hadron w.r.t. the virtual photon, in the center-of-mass frame of the proton (or ion) and virtual photon.

For exclusive processes, in addition to the scattered lepton, the final state photon in DVCS or meson in Deeply Virtual Meson Production as well as the scattered proton are measured. In this case, another kinematic variable is introduced – the squared momentum transfer to the proton, t, defined as

$$t \equiv (p' - p)^2 \tag{2.7}$$

where p' is the four-momentum of the scattered proton.

2.2   Inclusive DIS and scattered electron measurements

In inclusive DIS, where only the kinematics of the scattered electron are necessary, the primary requirements of any detector are electron identification and sufficient resolution in x and Q^2, which in turn mandates good energy and angle resolution for the scattered electron measurements (Eq. 2.2–2.4).

2.2.1   Electron Identification

In collider geometry, the DIS electrons are scattered mainly in the electron-going direction and central rapidities (barrel acceptance), see Figure 2.1. Central rapidity selects scatterings with higher Q^2 and higher x (due to its correlation with Q^2). The higher the electron beam energy, the more scattering there is in the electron-going direction. The energy of the scattered electron varies in the range from zero up to the electron beam energy and even to higher values for electrons detected in the barrel acceptance, see Figure 2.1.
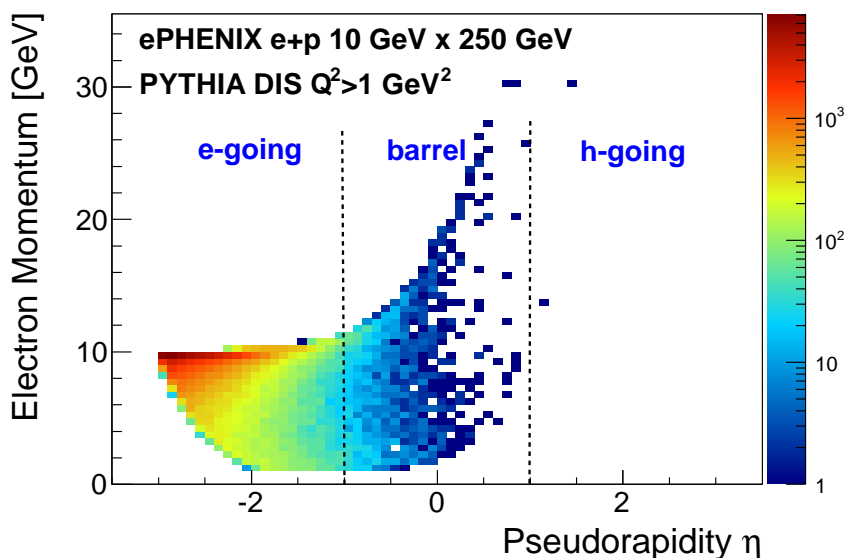

Figure 2.1: Shown is the distribution of scattered electrons in pseudorapidity and energy. The results are from PYTHIA DIS simulations for $e+p$ collisions with $10\,\mathrm{GeV} \times 250\,\mathrm{GeV}$ beam energies. The events are selected as DIS with $Q^2 > 1\,\mathrm{GeV}^2$.

Collider kinematics allow clear separation of the scattered electrons from other DIS fragments — hadrons and their decay products — which are detected preferably in the hadron-going direction, leaving much softer spectra in the central region and the electron-going direction. Figure 2.2 shows scattered electron momentum spectra along with photon (mainly from hadron decays) and charged pion spectra. For the 10 GeV electron beam, hadronic and photonic backgrounds are small above $\sim 5\,\mathrm{GeV/c}$, but increase rapidly at lower momenta.

The different response of the EMCal to hadrons and electrons, along with a direct comparison of energy deposited in the EMCal and momentum measured in the tracking system (i.e., E/p matching) provides a significant suppression of hadronic background in DIS scattered electron measurements: from a factor of 20–30 at momenta near $1\,\mathrm{GeV/c}$ to a factor of greater than 100 for momenta above $3\,\mathrm{GeV/c}$. Figure 2.3 shows the effectiveness
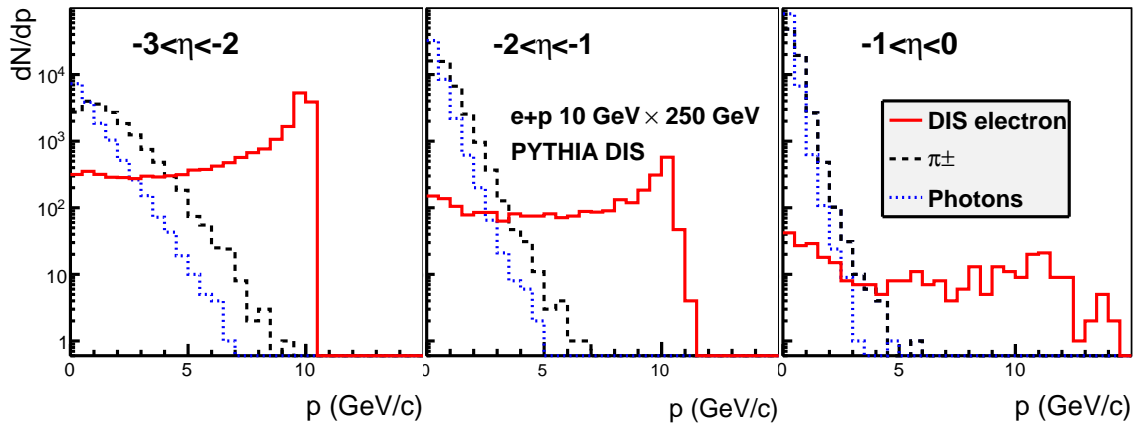
Figure 2.2: For 10 GeV $\times$ 250 GeV beam energy configuration: Momentum spectra for scattered electron (red), charged pions (black) and photons (blue).

of electron identification with the EMCal and tracking, providing high purity for DIS scattered electron measurements at momenta >3 GeV/c for the 10 GeV electron beam (and >1.5 GeV/c for the 5 GeV electron beam). The evaluations above are done with a parametrized response of the EMCal to hadrons and electrons, and EMCal and tracking resolutions described in Sections 3.3 and 3.2. Further enhanced electron identification is expected from the use of the transverse shower profile. We are also studying possible electron identification improvement with longitudinal segmentation in the crystal calorimeter in the electron-going direction. These are expected to move the detector capabilities for high purity electron identification down to 2 GeV/c (1 GeV/c) for 10 GeV (5 GeV) electron beam, which only marginally limits the (x, Q^2) space probed in our measurements, see Figure 2.4.

Photon conversion in material between the collision point and the tracker (mainly beam pipe, with thickness as small as 0.3% of radiation length) is not expected to contribute sizable background. Moreover, conversion electron-positron pairs will be well identified by our tracking system in the magnetic field and additionally suppressed by E/p matching cut. A detailed GEANT simulation study is ongoing to quantify this effect.

2.2.2 Resolution in x and Q^2 and bin survival probability

Measurements of the scattered electron energy and polar angle impact the DIS kinematic reconstruction, Eq. 2.2–2.4. Unfolding techniques are generally used to correct for smearing in (x, Q^2) due to detector effects, and the effectiveness of this technique depends on the degree to which events migrate from their true (x, Q^2) bin to another. This migration can be characterized by the likelihood of an event remaining in its true (x, Q^2) bin — the bin survival probability.
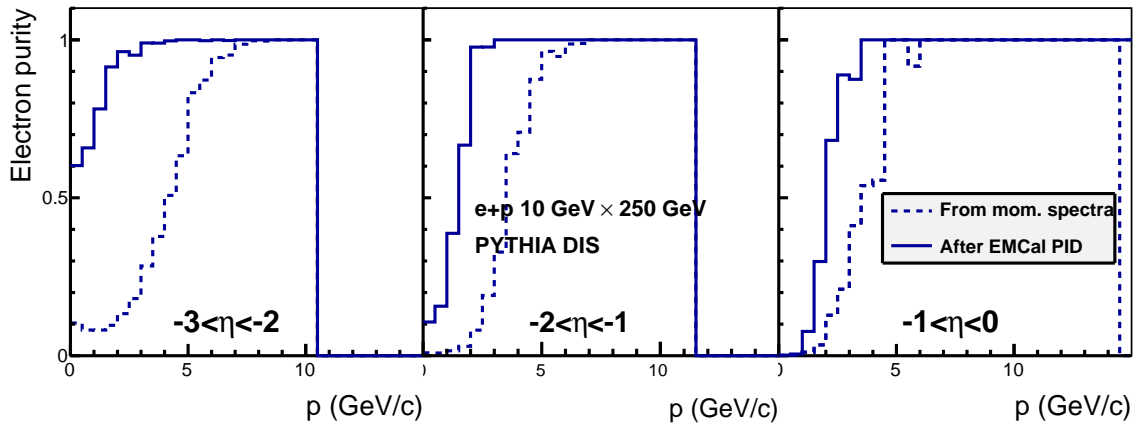
17

Figure 2.3: For 10 GeV × 250 GeV beam energy configuration: The fraction of charged particles from DIS electrons before electron identification (dotted) and after identification with the EMCal response and E/p matching (solid).

The energy resolution σ_E is directly propagated to σ_{Q^2}, so that $\sigma_{Q^2}/Q^2 = \sigma_E/E$. The EMCal energy and tracking momentum resolutions will provide excellent precision for Q^2 measurements. Conversely, the σ_x resolution is magnified by a factor of $1/y$ as $\sigma_x/x = 1/y \cdot \sigma_E/E$, and so the energy resolution in this approach effectively defines the limit of our kinematic reach at low y.

Figure 2.5 shows the relative resolution in Q^2 and x measurements using the standard "electron" method, in which the scattered electron is measured. While the Q^2 relative uncertainty, σ_{Q^2}/Q^2, is better than 10% over whole x-Q^2 acceptance, the relative uncertainty on x, σ_x/x, clearly demonstrates its y-dependence (the same y points are on the diagonal, as from Eq. 2.4, $Q^2 = syx$). The step in resolution around $Q^2 = 50\,\text{GeV}^2$ in these plots corresponds to the transition from the electron-going direction to the barrel acceptance, which differ mainly in the resolution of the different electromagnetic calorimeters covering those two regions of the acceptance. All of this translates to the statistics survival probability in a bin shown in Figure 2.6, which is calculated for five bins per decade in each of x and Q^2. The survival probability is $> 80\%$ for $y > 0.1$ in the electron-going direction and for $y > 0.3$ in the barrel acceptance.

The effect of the polar angle resolution θ in Eq. 2.2–2.4, is the biggest for forward scattering (small θ). It was found that crystal EMCal position resolution (better than 3 mm for > 1 GeV electrons, see Section 3.3.1) provides enough precision for scattered electron angle measurements, so that it affects the statistics migration in bins on Figure 2.6 only marginally.

The Jacquet-Blondel method using the hadronic final state is an alternative approach to reconstruct DIS kinematics. Its resolution for inelasticity y, and hence for x, is nearly flat, so it provides much better precision for x determination than the "electron" method, in
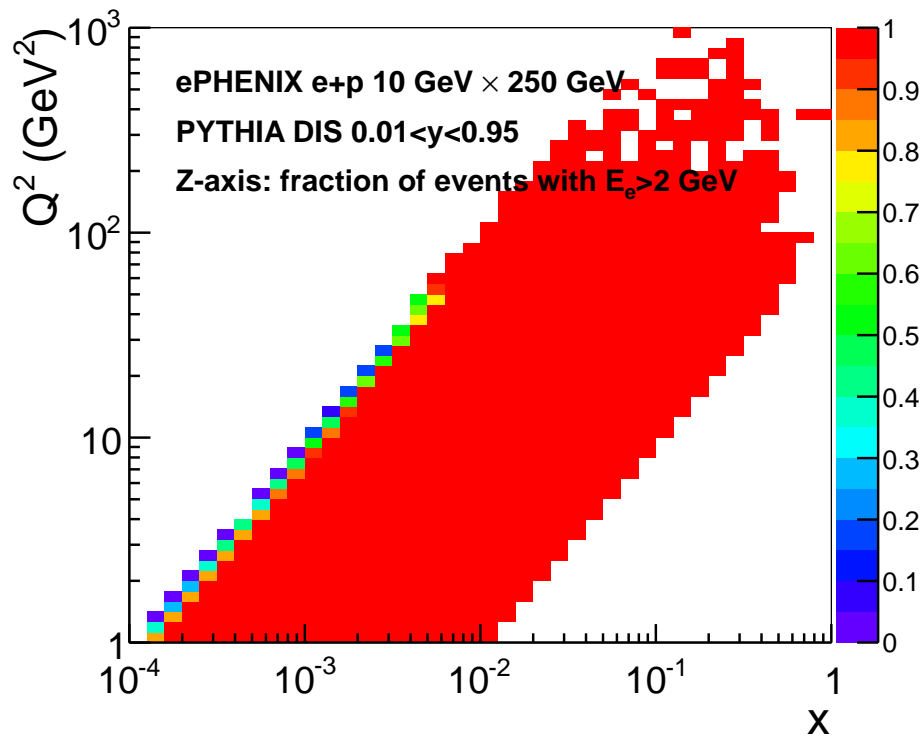
Figure 2.4: For 10 GeV $\times$ 250 GeV beam energy configuration: The color axis indicates the fraction of events in (x, Q^2) space surviving after a > 2 GeV energy cut on the DIS scattered electron.

the region with small y. It is also better in the higher Q^2 region corresponding to the barrel acceptance, where the resolution of the "electron" method is limited by the EMCal resolution.

The Jacquet-Blondel method requires the measurement of all final state hadrons produced in $e+p$ or $e+A$ scattering. A study with the PYTHIA generator shows that the precision of this approach does not deteriorate if the hadron detection capabilities are limited to $|\eta| < 4$. This method provides relative precision for the measurement of x of better than 20%, which satisfies the bin statistics migration criteria discussed above. It was found that for $y < 0.3$ the precision of this approach deteriorates only slightly when hadron measurements are limited to the barrel and forward acceptance $-1 < \eta < 4$ (the acceptances we plan to equip with hadron identification capabilities, see Section 3.5). As was shown above, measurements at higher y are well provided by the "electron" method.

Therefore, combining the electron and hadronic final state measurements provides precise determination of basic kinematic variable x, y and Q^2 in the whole kinematical space.

QED radiative effects (radiation of real or virtual photons) are another source of smearing
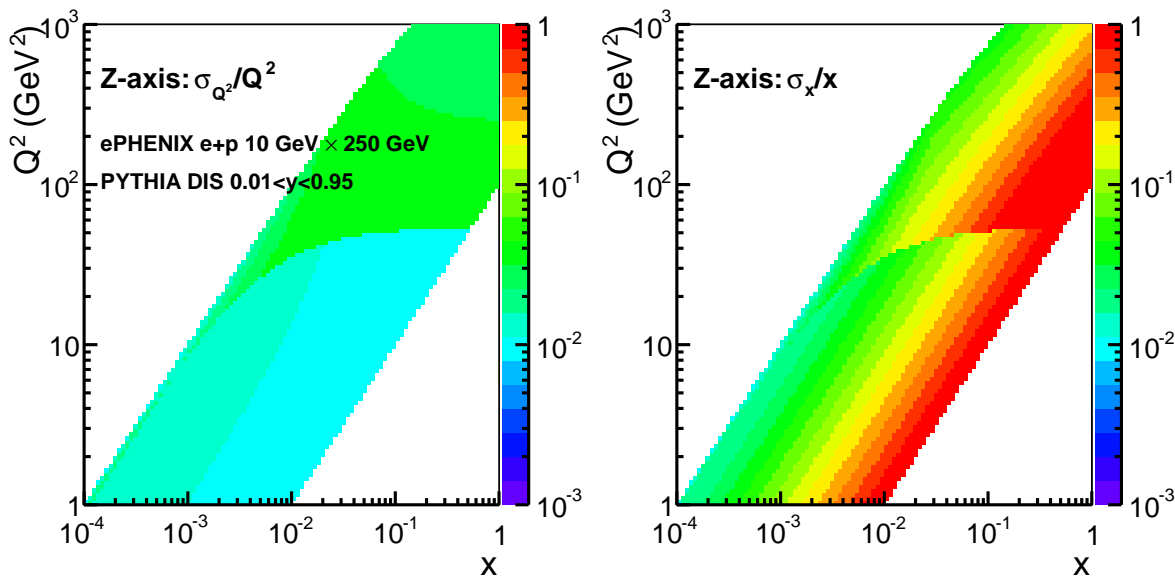
Figure 2.5: For 10 GeV × 250 GeV beam energy configuration: the relative resolution for Q^2 (left) and x (right) as a function of (x, Q^2).

which is usually corrected with unfolding techniques. Unlike energy-momentum resolutions which introduces Gaussian-like smearing, radiative corrections are tail-like. They can be responsible for as much as 10–20% of statistics migrating away from a bin, and dominate over energy-momentum smearing at higher y (compare to Figure 2.6).

2.3   Semi-inclusive DIS and hadron ID

As was discussed in Chapter 1, measurements of hadrons in SIDIS events are necessary to determine both the (sea)quark separated helicity distributions and TMDs. It is also important for understanding the hadronization process in nuclear matter. For these measurements, one needs to identify the hadron, particularly in the case of pions and kaons. In this section, we discuss the kinematic ranges of interest for pions, kaons and protons, and in Chapter 3, we discuss technology choices which can effectively make these measurements.

Figure 2.7 shows the yields of positively charged hadrons as a function of momentum and pseudorapidity for the 10 GeV × 250 GeV beam configuration. A minimum z cut of $z > 0.2$ to remove soft physics effects and beam remnant is applied. For $\eta < 0$, the hadron momenta are limited by the electron beam momentum, while in the hadron-going direction, the hadron momenta extend almost to the full proton beam energy. The results are similar for other beam energy configurations.
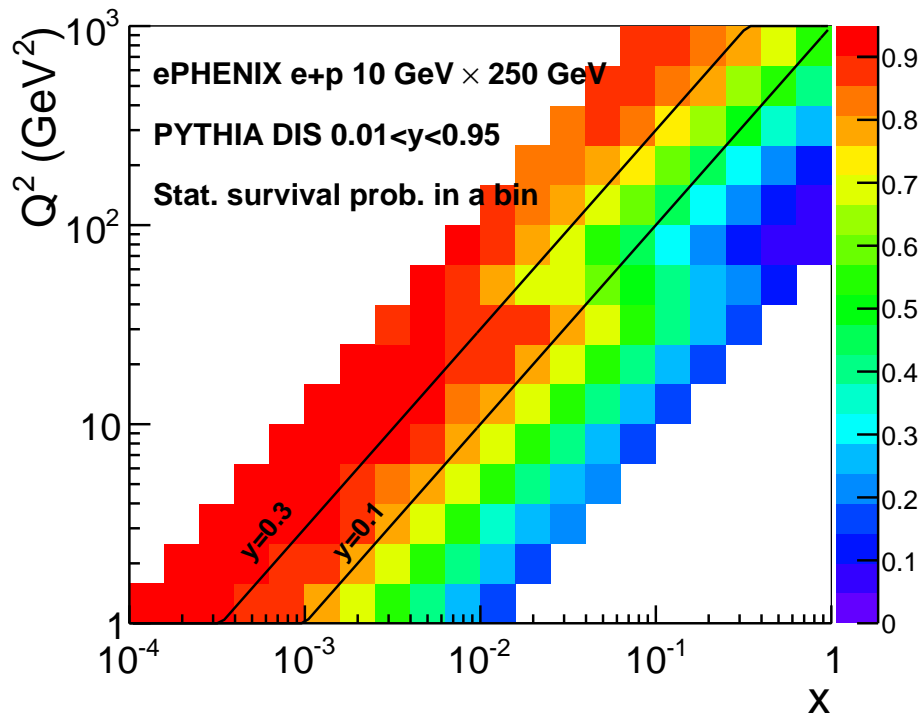
Figure 2.6: For 10 GeV × 250 GeV beam energy configuration: Statistics survivability in (x,Q^2) bins.

As was stated above, ePHENIX will have three PID systems: (1) a DIRC covering $|\eta| <$ 1 providing π-K separation below 3.5–4 GeV/c (depending on purity and efficiency requirements), (2) an aerogel based RICH covering $1 < \eta < 2$ providing π-K (K-p) separation below 6 (10) GeV/c and (3) a gas based RICH covering $1 < \eta < 4$ providing π-K separation for $3 < p < 50$ GeV/c and $K - p$ separation for $15 < p < 60$ GeV/c (depending on the balance between efficiency and purity chosen). Based on these numbers, the PID for kaons would cover the η and p region outlined in black in Figure 2.7. The resulting ePHENIX x and Q^2 coverage for SIDIS events with an identified kaon is shown in Figure 2.8, for low ($0.30 < z < 0.35$) and high ($0.70 < z < 0.75$) z bins, along with lines indicating the accessible DIS y range ($0.01 < y < 0.95$).

Figure 2.9 shows the impact on the x and Q^2 coverage of removing one of the three PID detectors planned for ePHENIX at low and high z. The plots show the ratio of kaon yields when using only two PID detectors to those with all three detectors (i.e., standard ePHENIX). If the gas-based RICH detector is removed (left), the high x reach, particularly at high Q^2, is lost. If the aerogel-based RICH is removed (middle), sensitivity to the region of moderate x, Q^2 and y is lost. Finally, if the DIRC is removed, significant kinematic coverage at low x, as well as moderate x and high Q^2 is lost. To achieve a wide x and Q^2
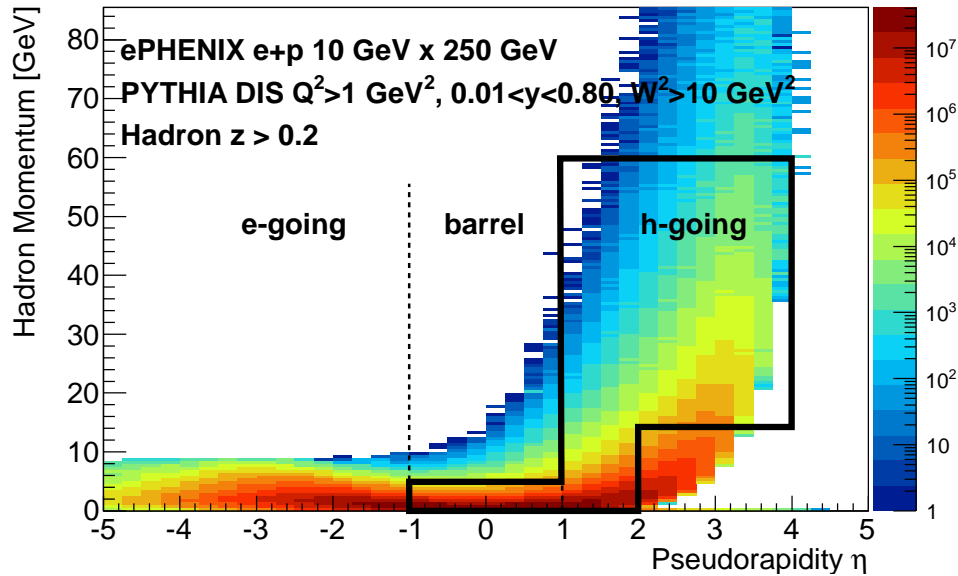
Figure 2.7: Shown is the distribution of hadrons from DIS events in $e+p$ as a function of momentum and pseudorapidity, based on PYTHIA simulations of the 10 GeV $\times$ 250 GeV beam energy configuration. The black outline indicates the pseudorapidity and momentum range covered for kaons by the planned PID detectors in ePHENIX.

coverage, all three detectors are necessary. Extending the aerogel-based RICH to $\eta > 2$ does not extend the kinematic coverage; the momentum range covered by such a detector corresponds to very low values of y.

2.4   Exclusive DIS

Among exclusive processes, Deeply Virtual Compton Scattering (DVCS) is of special interest (see Section 1.3.1). The produced DVCS photon energy versus pseudorapidity distribution is shown in Figure 2.10. Most of the photons fall in the electron-going direction and the barrel (central rapidity) acceptance. The photon energy for $-1 < \eta < 1$ varies in the range $\sim$ 1–4 GeV/c and is nearly independent of the beam energy in the range considered for eRHIC. Photons in the electron-going direction are more correlated with the electron beam and have energy from 1 GeV up to electron beam energy.

Figure 2.11 shows the x-Q^2 range covered by DVCS measurements for different rapidity ranges, emphasizing the importance of measurements over a wide rapidity range. Wide kinematical coverage is also important for separating DVCS events from Bethe-Heitler (BH) events (when a photon is radiated from the initial or final state lepton), which share
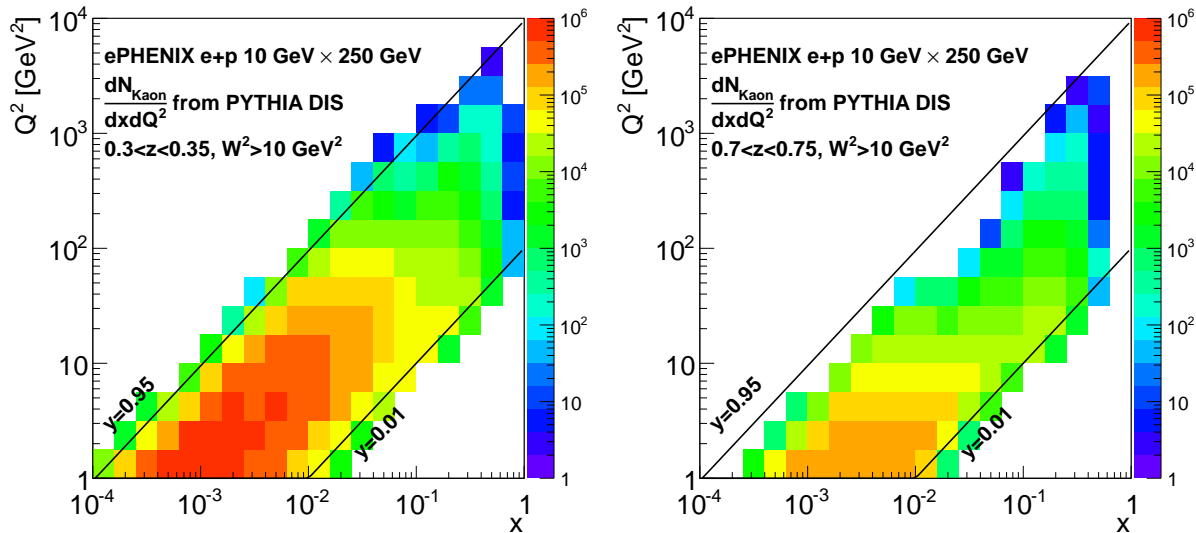
Figure 2.8: x and Q^2 distribution of events with kaons which can be identified with the ePHENIX PID detectors in expected binning at (left) low and (right) high z.

the same final state. This can be done by utilizing the different kinematic distributions of DVCS and BH photons (e.g., in rapidity and inelasticity y). The planned EMCal and tracking cover $|\eta| < 4$ (Section 3.3 and 3.2) and will provide excellent capabilities for DVCS measurements.

To ensure the reliable separation of electromagnetic showers in the EMCal from the scattered electron and the DVCS photon, sufficient EMCal granularity is necessary. The minimal angle separation between the electron and the photon is reached for electrons with the smallest scattering angle (i.e., the smallest Q^2) and is inversely proportional to electron beam energy. For a 10 GeV electron beam and $Q^2 > 1$ GeV^2, the minimum angle is ~ 0.1 rad. The proposed crystal EMCal in the electron-going direction, with granularity ~ 0.02 rad (see Section 3.3.1), will provide the necessary electron and photon shower separation.

It is also important to ensure the exclusiveness of the DVCS measurements, and so it is highly desirable to reconstruct the scattered beam proton. The proton scattering angle is inversely proportional to proton beam energy and varies from 0 to 5 mrad for 250 GeV proton beam and four-momentum transfer $-t < 1$ GeV^2. It can be detected with the planned "Roman Pots" detectors located along the beam line (See Section 3.6).

2.5   Diffractive measurements

Diffractive event measurements play an important role in nucleon and nucleus imaging. They are particularly sensitive to the gluon distribution in nuclei and hence to gluon
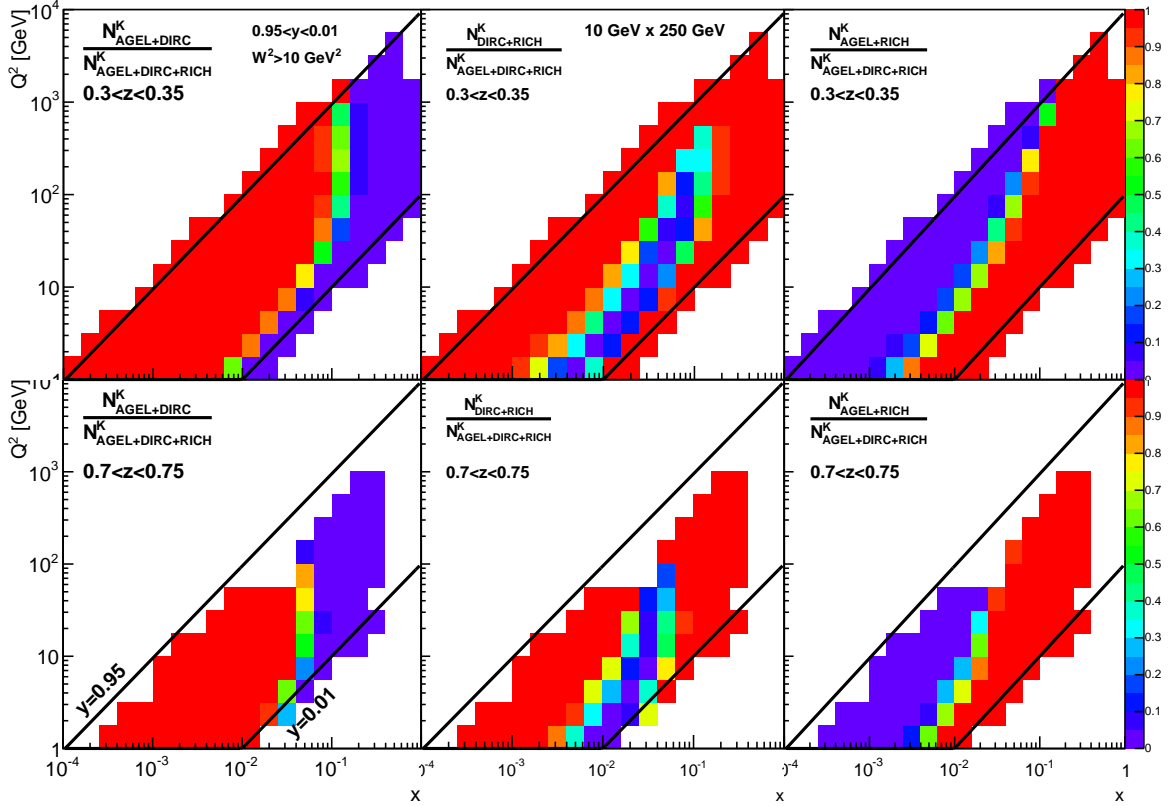
Figure 2.9: Efficiency as a function of x and Q^2 of kaon identification when comparing to baseline ePHENIX design with a DIRC, RICH and Aerogel when one of these subsystems is removed. The top three plots are for low z ($0.3 < z < 0.35$) and the bottom three are for high z ($0.7 < z < 0.75$). Also shown are lines indicating different values of y.

saturation phenomena. Diffractive events are characterized by a rapidity gap, i.e. an angular region in the direction of the scattered proton or nucleus devoid of other particles. Figure 2.12 shows the pseudorapidity distribution for the most forward going particle in DIS events and in diffractive events. Extending the forward acceptance of the detector to $\eta = 4$ and beyond is important if one is to have good capability using the rapidity gap method for detecting diffractive events and to separate them from DIS processes.

The planned ePHENIX EMCal and tracking coverage of $|\eta| < 4$ and hadronic calorimetry coverage of $-1 < \eta < 5$ are expected to provide excellent identification capabilities for diffractive events. In addition, to separate coherent (the nucleus remains intact) and incoherent (the nucleus excites and breaks up) diffractive events, we plan to place a zero degree calorimeter after the first RHIC dipole magnet (see Section 3.6), which is expected to be very efficient at detecting nuclear break-up by measuring the emitted neutrons.
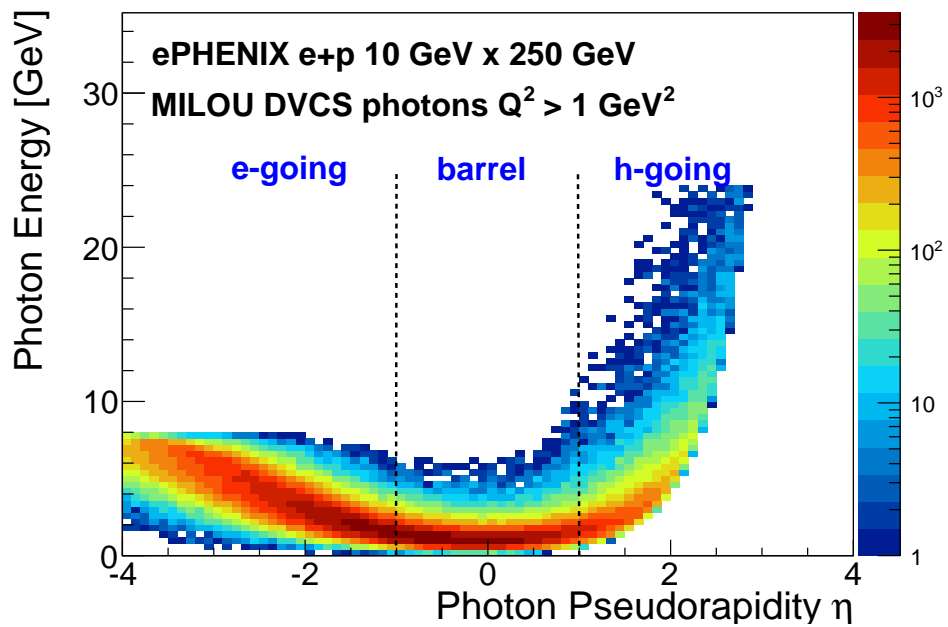
Figure 2.10: For the 10 GeV × 250 GeV beam energy configuration: DVCS photon energy vs pseudorapidity distribution; the *z*-axis scale shows the relative distribution of events from the MILOU event generator.
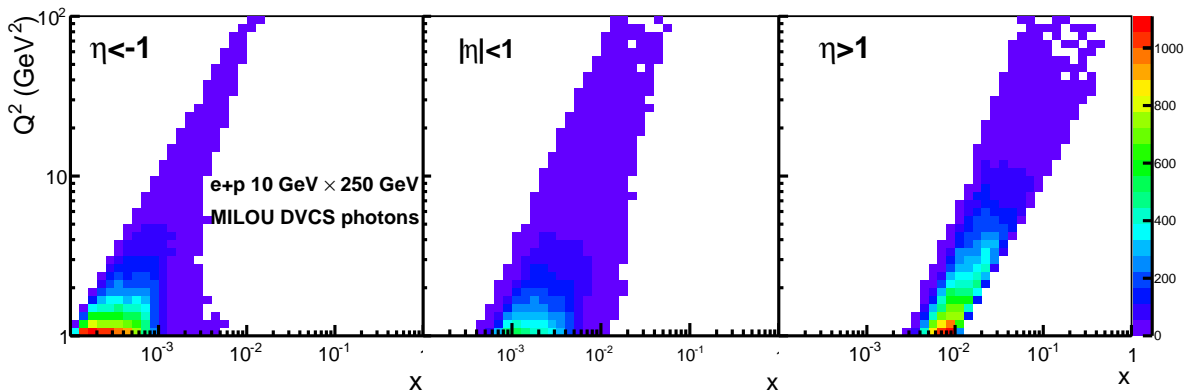
Figure 2.11: For 10 GeV × 250 GeV beam energy configuration: *x*-Q^2 coverage for DVCS events with photon detected in the electron-going direction, $\eta < -1$ (left), or central rapidities, $|\eta| < 1$ (middle) and hadron-going direction, $\eta > 1$ (right). The *z*-axis scale shows relative distribution of events from the MILOU event generator.
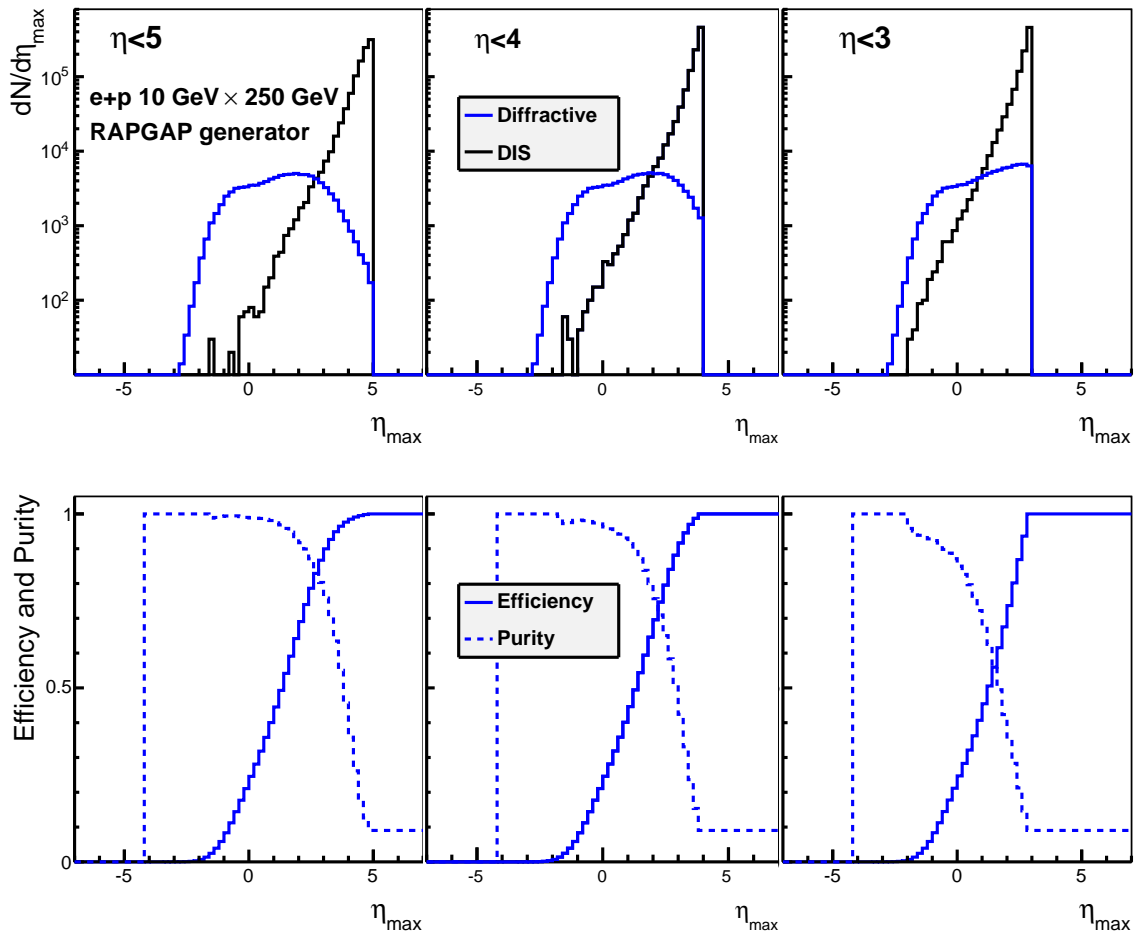
Figure 2.12: For the 10 GeV × 100 GeV beam energy configuration: Top: Pseudorapidity distribution for the most forward going particle in DIS events (black) and in diffractive events (blue); Bottom: Efficiency (dashed) and purity (solid) for diffractive event identification as a function of pseudorapidity cut defining the rapidity gap, for different detector acceptance: $|\eta| < 5$ (left), $|\eta| < 4$ (middle), $|\eta| < 3$ (right). Obtained using the RAPGAP generator developed at HERA and tuned to H1 and ZEUS data.

Chapter 3

Detector Concept
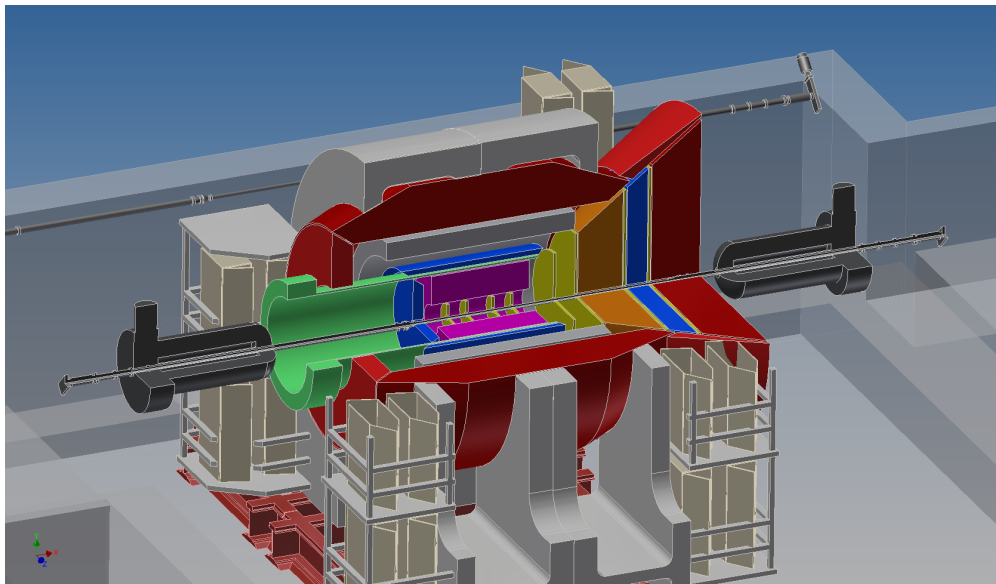
Figure 3.1: Engineering rendering of ePHENIX in the PHENIX experimental hall. The drawing shows the location of the final eRHIC focusing quadrupoles as well as the electron bypass beamline behind the detector.

A full engineering rendering of ePHENIX is shown in Figure 3.1. The drawing shows the ePHENIX detector in the existing PHENIX experimental hall and illustrates the reuse of the superconducting solenoid and the electromagnetic and hadronic calorimeter system of sPHENIX. The rendering also shows the final eRHIC focusing quadrupoles, each located 4.5 m from the interaction point (IP). Those magnets and the height of the beam pipe above the concrete floor, set the dominant physical constraints on the allowable dimensions of ePHENIX. This Chapter will describe the ePHENIX detector concept in terms of its component subdetectors and their expected performance.

The ePHENIX detector consists of a superconducting solenoid with excellent tracking
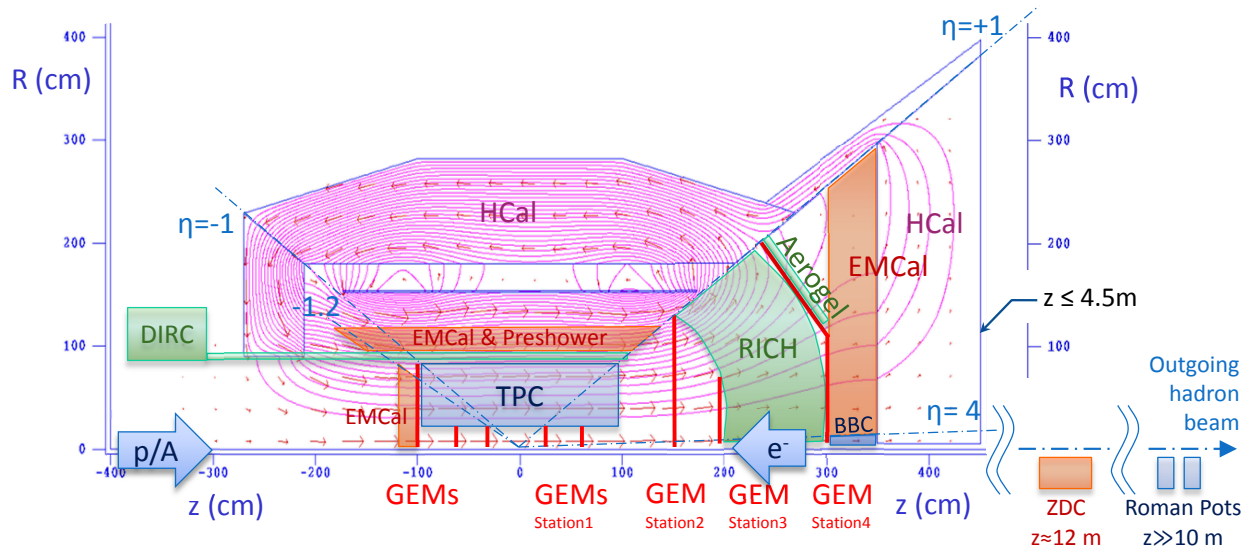
Figure 3.2: A cross section through the top-half of the ePHENIX detector concept, showing the location of the superconducting solenoid, the barrel calorimeter system, the EMCal in the electron-going direction and the system of tracking, particle identification detectors and calorimeters in the hadron-going direction. Forward detectors are also shown along the outgoing hadron beamline. The magenta curves are contour lines of magnetic field potential as determined using the 2D magnetic field solver, POISSON.

and particle identification capabilities covering a large pseudorapidity range, as shown in Figure 3.2. It builds upon an excellent foundation provided by the proposed sPHENIX upgrade [1] detailed in the MIE proposal submitted to the DOE Office of Nuclear Physics by Brookhaven National Laboratory in April 2013. The strong sPHENIX focus on jets for studying the strongly-coupled quark-gluon plasma in $p+p$, $p/d+$A and A+A is enabled by excellent electromagnetic and hadronic calorimetry in the central region ($|\eta| < 1$).

The C-AD Interaction Region (IR) design at the time the Letter of Intent charge was issued had the final focusing quadrupoles of the accelerator positioned ± 4.5 m from the IP and employed a "crab crossing" to maintain high luminosity while allowing the electron and hadron beams to intersect at an angle of 10 mr (see Figure 3.14). The ePHENIX detector concept shown in Figure 3.1 and Figure 3.2 respects these constraints. For instance, the hadronic calorimeter in the hadron-going direction fits within the 4.5 m constraint imposed by the accelerator magnets, and the detector is aligned so that the electron beam travels along the symmetry axis of the magnetic field. Clearly, the progress of ePHENIX from

concept to final design will be done in close consultation with C-AD to ensure that the design of IR and the design of the detector remain synchronized.

We have an extensive GEANT4 description of the ePHENIX detector, based on the same software framework as used in PHENIX and sPHENIX, which enables ready use of many existing PHENIX software analysis tools. An example of running a DIS event through the GEANT4 detector description is shown in Figure 3.3.
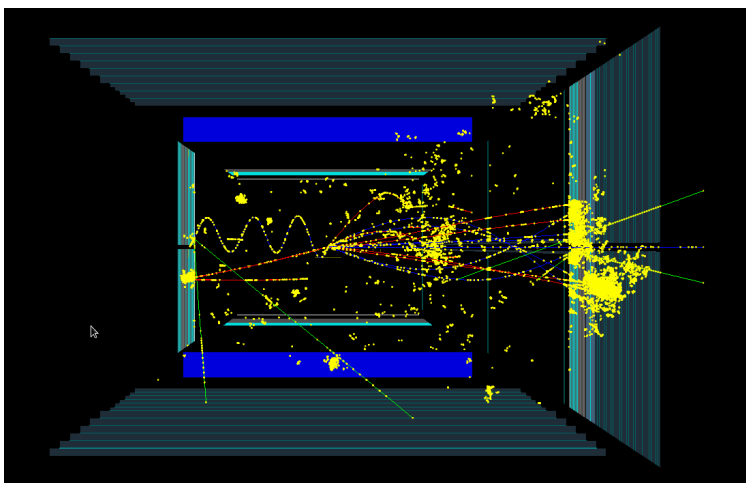
Figure 3.3: The response of the ePHENIX detector to a single event, as determined using GEANT4. The field map in this simulation was determined using the 2D magnetic field solver OPERA. These same OPERA calculations were used to verify and validate the calculations underlying the magnetic field lines shown in Figure 3.2.

The DOE funded sPHENIX subsystems which will be reused in ePHENIX are:

Superconducting solenoid: The sPHENIX detector concept reuses the BaBar superconducting solenoid to provide a 1.5 Tesla longitudinal tracking magnetic field. Its field is shaped in the forward directions with an updated yoke design in the ePHENIX detector as discussed in Section 3.1.

Electromagnetic calorimeter: A tungsten-scintillator sampling electromagnetic calorimeter with silicon photomultipliers (SiPMs) enables a compact barrel calorimeter positioned inside the bore of the superconducting solenoid. The calorimeter system provides full azimuthal coverage for $|\eta| < 1$ with an energy resolution of $\sim 12\%/\sqrt{E}$. The readout is segmented into towers measuring roughly $\Delta\eta \times \Delta\phi \sim 0.024 \times 0.024$.

Hadronic calorimeter: A $5\lambda_{\text{int}}$-depth hadron calorimeter surrounds the solenoid. An iron-plate and scintillator sampling design provides an energy resolution of better than $\sim 100\%/\sqrt{E}$ with full azimuthal coverage. It also serves as part of the magnetic flux return for the solenoid.

Table 3.1: Main characteristics of BaBar solenoid [14]

Central Induction	1.5 T
Winding structure	2 layers, 2/3 higher current density at both ends
Winding axial length	3512 mm
Winding mean radius	1530 mm
BaBar operation current	4596 A, 33% of critical current
Total turns	1067

In addition, new subsystems will be added to the ePHENIX detector, which will be further discussed in this Chapter. These subsystems include:

Electron going direction: GEM detectors [12, 13] and lead-tungstate crystal electromagnetic calorimeters

Central barrel: Fast, compact TPC tracker and DIRC

Hadron going direction: GEM tracking system, gas-based RICH, aerogel-based RICH, beam-beam counter (BBC), electromagnetic and hadron calorimeter

Beam line of hadron-going direction: Roman pot detectors and a zero-degree calorimeter

3.1   Magnet system

As with sPHENIX, ePHENIX is based around the BaBar superconducting solenoid [14] with no modifications to its inner structure. The major specifications for its coil are listed in Table 3.1. A notable feature of the BaBar magnet is that the current density of the solenoid can be varied along its length, i.e., lower current density in the central region and higher current density at both ends. This is accomplished by using narrower windings (5 mm) for the last 1 m at both ends. The central winding uses 8.4 mm-width coils [14]. The main purpose of the graded current density is to maintain a high field uniformity in the bore of the solenoid, which is also a benefit for ePHENIX. This design feature enhances the momentum analyzing power in both the electron-going and hadron-going directions.

A magnetic flux return system, consisting of the forward steel/scintillator hadron calorimeter, a flaring steel lampshade, and a steel endcap not only returns the flux generated by the
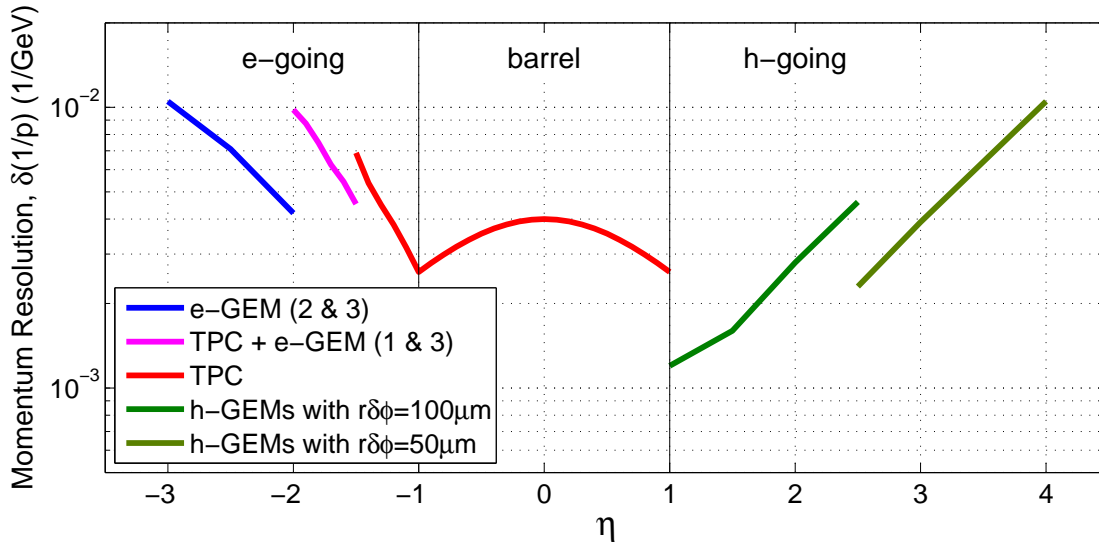
Figure 3.4: Momentum resolution over the full pseudorapidity coverage of the planned tracking system in the high momentum limit. Multiple scattering contribution to the relative momentum resolution (not shown on the plot) was studied with GEANT4 simulation, and found to vary from below 1% at low pseudorapidity to $\sim$3% at $|\eta|$=3.

solenoid, but shapes the field in order to aid the momentum determination for particles in the hadron-going and electron-going directions. As shown in Figure 3.2, the flux return system consists of the following major components:

- Forward steel/scintillator hadron calorimeter, at $z = 3.5$ to 4.5 m

- Steel flux shaping lampshade, along the $\eta \sim 1$ line

- Barrel steel/scintillator hadron calorimeter, from $r = 1.8$ to 2.8 m

- Steel end cap, at $z = -2.1$ to -2.7 m and $r > 90$ cm

The magnetic field lines were calculated and cross checked using three different 2D magnetic field solvers (POISSION, FEM, and OPERA) and are shown in Figure 3.2. In the central region, a 1.5 Tesla central field along the electron beam direction is produced. The field strength variation within the central tracking volume is less than $\pm$3%.

3.2   Vertex and Tracking

The z-location of the primary event vertex will be determined using a timing system enabling a precision of $\Delta z \leq 5$ mm. The ePHENIX tracking system utilizes a combination of GEM and TPC trackers to cover the pseudorapidity range of $-3 < \eta < 4$. The momentum resolution for the full device is summarized in Figure 3.4.

3.2.1   Event vertex measurement

The vertex information is used for the determination of photon kinematics and for assisting the track fitting. Precise vertex information is important for momentum determination in the electron-going direction, where tight space constraints limit the possible number of tracking planes. The location of the vertex will be measured by:

- For non-exclusive processes, we propose to identify the z-location for the vertex using timing information from a BBC detector in the hadron-going direction in coincidence with the electron beam RF timing. The BBC detector covers $\eta = 4$–5 at $z = 3.0$ m. A timing resolution of 30 ps or better enables the measurement of the vertex with resolution of $\Delta z = 5$mm. It leads to a sub-dominant error for the momentum determination for the electron-going direction ($\delta p/p = 2\%$). This timing resolution can be provided by the existing technology of Multigap Resistive Plate Chamber (MRPC) [15] or by microchannel plate detectors (MCP) photomultiplier [16] with a thin quartz Čerenkov radiator, a technology which is under active current development.

- We plan to measure the average transverse beam position by accumulating tracking information over the course of a one hour run. The statistical precision for the beam center determination is expected to be much smaller than the distribution of the transverse collision profile ($\sigma_{x,y} \sim 80~\mu$m), and therefore a negligible contribution to the uncertainty for event-by-event vertex determination.

3.2.2   Tracking in the central region, $-1 < \eta < 1$

A fast, compact Time Projection Chamber (TPC) will be used for tracking in the central region, occupying the central tracking volume of $r = 15$–80 cm and $|z| < 95$ cm and covering $-1 < \eta < 1$. A TPC will provide multiple high resolution space point measurements with a minimal amount of mass and multiple scattering. The design is based on a GEM readout TPC, similar to a number of TPCs that have either already been built or are currently under design. For example, the LEGS TPC [17] utilized a fine chevron-type readout pattern with a pad size of 2 mm $\times$ 5 mm and achieved a spatial resolution $\sim 200~\mu$m. The use of such a readout pattern helps minimize the total channel count for the electronics and hence the total cost. The GEM TPC upgrade for ALICE [18, 19] and the large GEM readout TPC for ILC [20, 21] are other examples of large GEM TPCs that have recently been studied.

It is assumed that the TPC will have a single high voltage plane at $z = 0$ cm and be read out on both ends, resulting in a maximum drift distance ~ 95 cm. It will use a gas mixture with a fast drift time, such as 80% argon, 10% CF_4 and 10% CO_2, which, at an electrical field of 650 V/m, achieves a drift speed ~ 10 cm/μs, and would result in a maximum drift time of 10 μs. With a position resolution of $\sigma(r\Delta\phi) = 300~\mu$m and 65 readout rows, the

expected transverse momentum resolution would be $\delta(1/p_T) = 0.4\%/(\text{GeV}/c)$ for high momentum tracks.

3.2.3 Tracking in hadron-going direction, $\eta > 1$

The design of the magnetic flux return enables tracking in the hadron-going direction in the main and fringe fields of the BaBar magnet. Compared to a compact solenoid with no current density gradient, the BaBar magnet system improves the momentum analyzing power for forward tracks by about a factor of four due to two main factors: 1) the BaBar magnet has a length of 3.5 m, which provides a longer path length for magnetic bending; 2) the higher current density at the ends of the solenoid improves the magnetic field component transverse to forward tracks, and therefore provides higher analyzing power.

The tracking system at high η in the hadron-going direction utilizes four stations of GEMs.

- Station 1 consists of two planes with complementary η coverages. They are located at $z = 17$ and 60 cm, respectively, covering a radius of $r = 2$–15 cm.

- Stations 2–4 are at $z = 150, 200, 300$ cm, respectively, covering $\eta = 1$–4.

The readout planes for these devices are optimized to preserve high position resolution in the azimuthal direction ($\sim 200~\mu$m in $r\delta\phi$ using a chevron-type readout with a pad size similar to the central TPC) and $\sim$10–100 mm in δr, while minimizing the readout channel cost. However, the r-ϕ resolution can be improved to be better than 100 μm, even for tracks at larger angles (up to 45 degrees), by the use of mini-drift GEM detectors, in which a small track segment, or vector, is measured for each track at each measuring station. These detectors, which are currently under development [22], would provide improved position resolution with less material and lower cost than multiple stations of planar GEM detectors. For this letter, we assumed that a high resolution GEM readout pattern (1 mm wide chevron-type readout) with a $r\delta\phi \sim 50~\mu$m for the inner tracking region ($\eta > 2.5$). For the outer tracking region ($1 < \eta < 2.5$), mini-drift GEM with 2 mm chevron-type readout provide $r\delta\phi \sim 100~\mu$m. The momentum resolution is estimated in Figure 3.4.

It should be noted that the size of the GEM trackers for Stations 2–4 are quite large (~ 5–20 m^2). It is currently challenging to produce such large GEM foils and to do so at an affordable cost. However, there has been substantial progress in this area in recent years at CERN due to the need for large area GEM detectors for the CMS Forward Upgrade [23]. CERN has developed a single mask etching technology which allows fabrication of very large area GEMs (up to 2 m $\times$ 0.5 m), and they plan to transfer this technology to various commercial partners (such as Tech Etch in the US, which supplied the GEM foils for the STAR Forward GEM Detector). We anticipate being able to procure such large area GEM detectors by the time they are needed for EIC.

3.2.4   Tracking in the electron-going direction, $\eta < -1$

The electron direction tracking is designed to fit in the space limited by the DIRC ($R <$ 80 cm) and the electromagnetic calorimeter ($z > -100$ cm). Three GEM tracking stations, located at $z = 30$, 55 and 98 cm, are used in combination with the TPC and vertex information to determine the momentum vector.

- For $\eta = -1.5$ to -1, TPC track segment and vertex are used

- For $\eta = -2.0$ to -1.5, vertex, TPC track segment, GEM station 1 and 3 are used.

- For $\eta = -3.0$ to -2.0, vertex, GEM station 2 and 3 are used.

Similar to the hadron-going direction, the position resolution for these detectors is $r\Delta\phi$ 50 μm for $-3 < \eta < -2$ using 1 mm wide chevron-type readout. For $-2 < \eta < -1$, the mini-drift GEM technology [22] and 2 mm wide chevron-type readout provide $r\delta\phi \sim$ 100 μm. The radial resolution is $\delta r = 1$ cm (stations 1 and 2) and $\delta r = 10$ cm (station 3). As shown in Figure 3.4, a momentum resolution of $\Delta p / p < 5\%$ can be achieved for tracks of $p < 4\,\text{GeV}/c$ and $-1 < \eta < -3$, which is sufficient for the calorimeter E-p matching cut for the electron identification. For DIS kinematics reconstruction the tracking radial resolution is not crucial as enough precision for scattered electron polar angle measurements will be provided by the EMCal, see Section 2.2.2.

3.3   Electromagnetic calorimeters

The ePHENIX detector will have full electromagnetic calorimeter coverage over $-4 < \eta < 4$. The sPHENIX barrel electromagnetic calorimeters will also be used in ePHENIX, covering $-1 < \eta < 1$ with an energy resolution of $\sim 12\%/\sqrt{E}$. In addition, crystal and lead-scintillator electromagnetic calorimeter are planned for the electron-going and hadron-going direction, respectively. Optimization of the design of the barrel and endcap calorimeters will aim for uniform response in the overlap region between $-1.2 < \eta < -1$.

3.3.1   Crystal Electromagnetic calorimeter

The calorimeter on the electron-going side consists of an array of lead tungstate ($PbWO_4$) crystals (commonly known as PWO), similar to the PANDA endcap crystal calorimeter shown in Figure 3.5 [24]. An enhanced light output version of lead tungstate (PWO-II) was chosen to provide high light yield (~ 20 p.e./MeV at room temperature) at a moderate cost ($\sim €5/\text{cm}^3$). It will provide an energy resolution $\sim 1.5\%/\sqrt{E}$ and position resolution better than $3\,\text{mm}/\sqrt{E}$ in order to measure the scattered electron energy and angle in the electron-going direction down to low momentum with high precision.
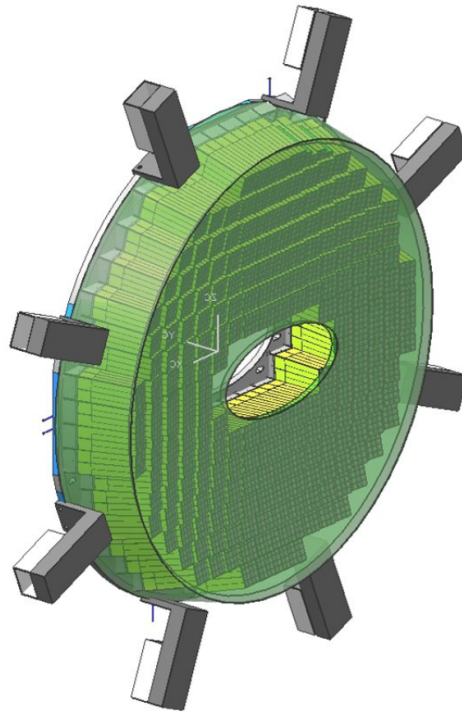
Figure 3.5: PANDA Crystal Endcap Calorimeter [24]. The PWO crystal modules are shown in green color, which is projective towards the target.

The ePHENIX PWO calorimeter will consist of $\sim$ 5000 crystals, compared with 4400 crystals for the PANDA endcap, and will have a similar size and shape to the PANDA crystals. They will be $\sim$ 2 cm $\times$ 2 cm (corresponding to one R_M^2) and will be read out with four SiPMs. This is different than the PANDA readout, which uses large area ($\sim$ 1 cm^2) APDs. The SiPMs will provide higher gain, thus simplifying the readout electronics, and will utilize the same readout electronics as the other calorimeter systems in sPHENIX. It is also expected that the cost of SiPMs will be less than that of APDs covering the same area by the time they are needed for ePHENIX.

3.3.2   Lead-scintillator electromagnetic calorimeter

The electromagnetic calorimeter in the hadron-going direction consists of a lead-scintillating fiber sampling configuration, similar to the tungsten-scintillating fiber calorimeter in the central sPHENIX detector. Lead is used instead of tungsten in order to reduce the cost, but it is otherwise assumed to be of a similar geometry. It will cover the rapidity range from $1 < \eta < 4$ and have 0.3 X_0 sampling (2 mm lead plates) with 1 mm scintillating fibers, which will give an energy resolution $\sim$ 12%/$\sqrt{E}$. The segmentation and readout will also be similar to the central tungsten calorimeter, with $\sim$ 3 cm $\times$ 3 cm towers (roughly 1 R_M^2) that are read out with SiPMs. This segmentation

(a) Aerogel and RICH gas radiators for hadron-going direction

(b) Fused silica radiator for barrel DIRC detector. Data are measured by the BaBar DIRC [25]
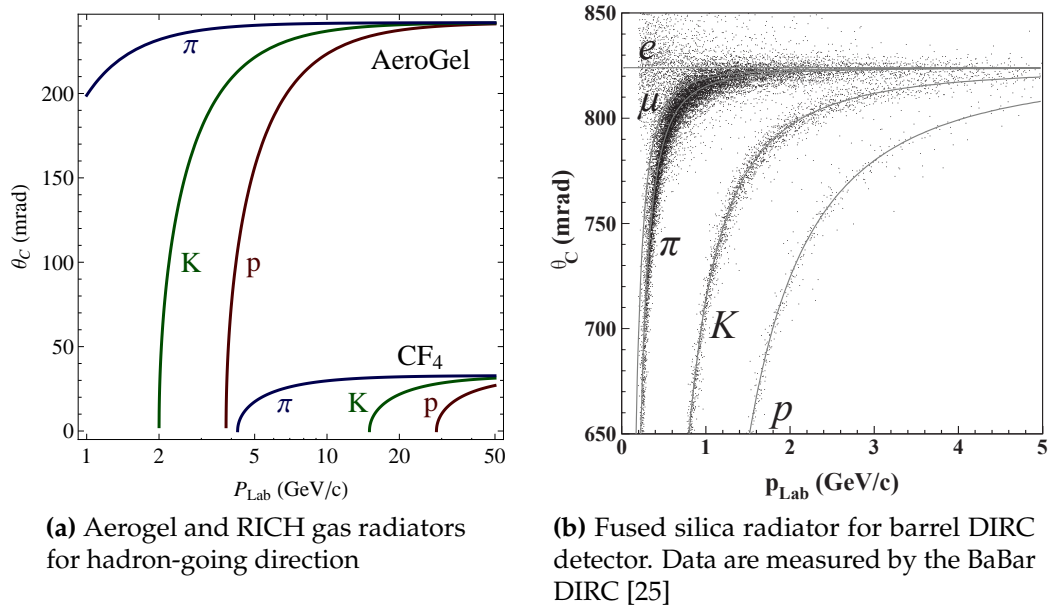
Figure 3.6: Čerenkov angle versus momentum for various particle species.

leads to $\sim 26K$ towers. By using the same type of readout as the central calorimeter, the front end electronics and readout system will also be similar, resulting in an overall cost savings for the combined calorimeter systems.

3.4   Hadron calorimeter

The hadron calorimeter in the hadron-going direction consists of a steel-scintillating tile design with wavelength shifting fiber readout, similar to the central sPHENIX hadron calorimeter. It will be $\sim 5 \, L_{abs}$ thick and cover a rapidity range from $1 < \eta < 5$. The steel in the absorber will also serve as part of the flux return for the solenoid magnet. The segmentation will be $\sim 10 \, cm \times 10 \, cm$, resulting in ~ 3000 towers. The readout will also be with SiPMs, similar to the central sPHENIX HCAL, which will again provide an advantage in being able to use a common readout for all of the calorimeter systems.

3.5   Hadron PID detectors

Hadron PID is planned for the hadron-going and barrel regions, covering $-1.2 < \eta < 4$. In the hadron-going direction, two PID detectors cover complementary momentum range: a gas-based RICH detector for the higher momentum tracks and an aerogel-based RICH

Figure 3.7: The cross-section of the gas-based RICH detector in the *r-z* plane that crosses the mirror center. The interaction point is centered at $(0,0)$. The geometric center of the mirror is shown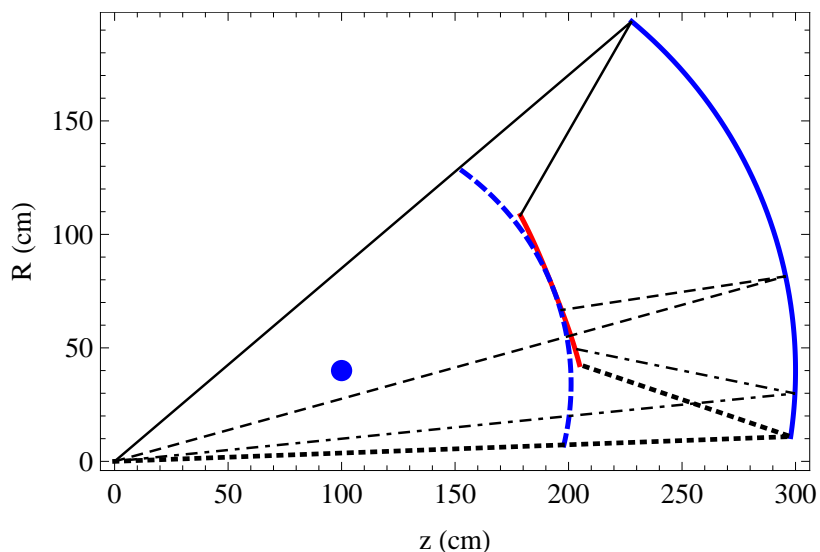 as the blue dot at $(r,z) = (40 \, \text{cm}, 100 \, \text{cm})$. The mirror and RICH entrance window are shown by the solid and dashed blue curves, respectively. Several example tracks and the central axis of their Čerenkov light cone are illustrated by the black lines. The Čerenkov photons are reflected by the mirror to the focal plane, shown in red.

detector for the lower momentum region. As in the BaBar experiment [25], a DIRC detector identifies hadron species in the central barrel. In addition, the TPC detector assists with PID by providing dE/dx information for the low momentum region.

3.5.1 Gas RICH detector

High momentum hadron PID is provided by an optically focused RICH detector using a gas radiator. The main features for this RICH setup are

- One meter of CF_4 gas is used as the Čerenkov radiator. The pion, kaon and proton thresholds are 4, 15 and 29 GeV, respectively.

- Čerenkov photons are focused to an approximately flat focal plane using spherical mirrors of 2 m radius, as shown in Figure 3.7. The geometric center of the mirror is at $(r,z) = (40 \, \text{cm}, 100 \, \text{cm})$, as highlighted by the blue dot.

- There are six azimuthal segmented RICH sextants.

- The photon detector consists of CsI-coated GEM detectors [26], which are installed on the focal plane. The CsI coating converts the Čerenkov photons into electrons which are then amplified by the GEM layers and readout through mini-pads. The
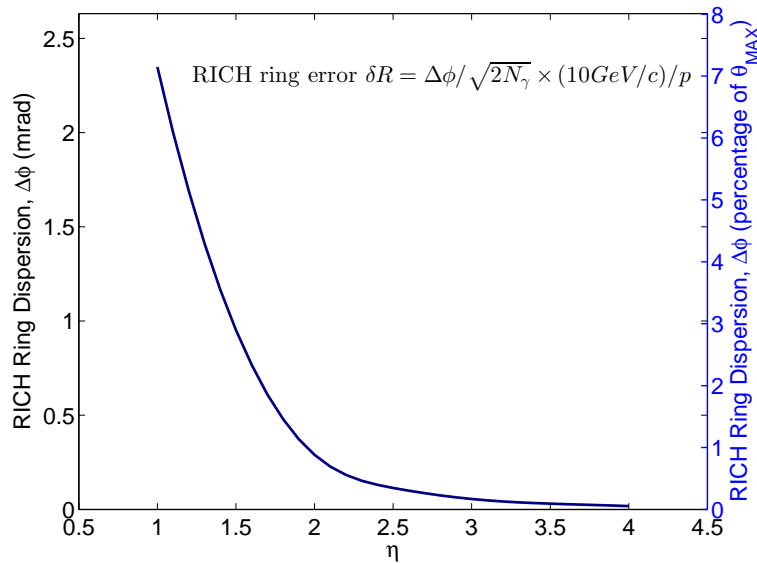
Figure 3.8: Azimuthal angular dispersion of gas-based RICH ring due to fringe magnetic field for a $p = 10\,\text{GeV}/c$ track. It is compared to the maximum RICH ring angle as shown on the right vertical axis.

photon detector for each RICH sextant assumes a roughly triangle shape and covers an area of 0.3 m^2.

Two distortion effects were estimated to be sub-dominant in error contributions for most cases:

- Strong residual magnetic field ($\sim$ 0.5 Tesla) are present in the RICH volume. This field will bend the tracks as they radiate photons, and therefore smear the Čerenkov ring in the azimuthal direction. However, the field design ensures that the field component is mostly parallel to the track inside RICH and therefore this smearing effect is minimized. The RMS size of the smearing, $\Delta\phi$, is evaluated as in Figure 3.8. The uncertainty contribution to the RICH ring angular radius is $\delta R = \Delta\phi/\sqrt{2N_\gamma}(10\,\text{GeV}/c)/p$, which is sub-dominant comparing to the photon measurement error for $\eta > 1.5$. The field contribution was included in the RICH performance estimation.

- For tracks that originate from an off-center vertex, their focal point may be offset from the nominal focal plane as shown in Figure 3.7. The effect is η dependent. For the most extreme case, that a track of $\eta = 1$ originates from the vertex of $z = 40$ cm (1.5 sigma of expected vertex width), an additional relative error of $5\%/\sqrt{N_\gamma}$ is contributed to the ring radius measurement, which averages over all vertices to below $2\%/\sqrt{N_\gamma}$ contribution. For high η tracks, the difference is negligible comparing to the nominal RICH error.

We simulated the RICH performance with a radiator gas CF_4 (index of refraction 1.00062). We use PYTHIA to generate the momentum distributions for pions, kaons, and protons. For each particle species, we use the momentum resolution and RICH angular resolution, to calculate the particle mass $m(p, \theta_{Crk})$ distribution. For higher momentum tracks the combined information from tracking system and energy deposit in HCal helps to improve momentum resolution particularly at higher rapidities, where momentum resolution from tracking degrades. For example, at pseudorapidity η=4, the tracking momentum resolution for 50 GeV/c tracks is $\sim$50% (see Figure 3.4), while HCal can provide energy measurements with precision $100\%/\sqrt{50[\text{GeV}]} \sim 14\%$. Our simulation showed that the HCal is very effective in improving the resolution for high momentum track measurements even when this and other tracks (usually with lower momenta) are merged in a single cluster of deposited energy in HCal. In such a case, the contribution of lower energy tracks in HCal can be evaluated and subtracted based on momentum measurements in tracking system.

Figure 3.9 shows mass distributions for the most challenging high rapidity region η=4 for different reconstructed track momenta. We make a symmetric 90% efficiency cut on the mass distributions, and calculate the purity for π, K, p, shown in Figure 3.10. One can see high purity for all particle species up to momenta $\sim$50 GeV/c. Introducing asymmetric cuts on the mass distributions (and sacrificing some efficiency) extends further our capabilities for high purity hadron identification.

It is notable that the limitation on the mass resolution comes from the estimated 2.5% radius resolution per photon for the RICH from the EIC R&D RICH group. Our calculation includes the effect of the magnetic field distortion mentioned above, which is sub-dominant. This is a somewhat conservative estimate and LHCb and COMPASS have quoted values near 1% per photon. The R&D effort is working towards the best radius resolution, though there are challenges in having the light focus and readout within the gas volume in this configuration compared with LHCb or COMPASS.

3.5.2   Aerogel RICH detector

The aerogel detector will provide additional particle ID for kaons in the momentum range $\sim$ 3–15 GeV/c when used in conjunction with the gas RICH. Pions can be identified by the signal they produce in the gas RICH starting at a threshold of $\sim$ 4 GeV/c, and kaons will begin producing a signal in the aerogel at a threshold $\sim$ 3 GeV. Reconstructing a Čerenkov ring in the aerogel enables one to separate kaons from protons up to a momentum $\sim$ 10 GeV/c with reduced efficiency above that.

Measuring a ring in the aerogel detector is a challenging technical problem for a number of reasons. Due to its relatively low light output, it will require detecting single photons in the visible wavelength range with high efficiency inside the rather strong fringe field of the superconducting solenoid. Also, due to the limited space available, it is difficult to have a strong focusing element in the RICH to focus the light into a ring in a short
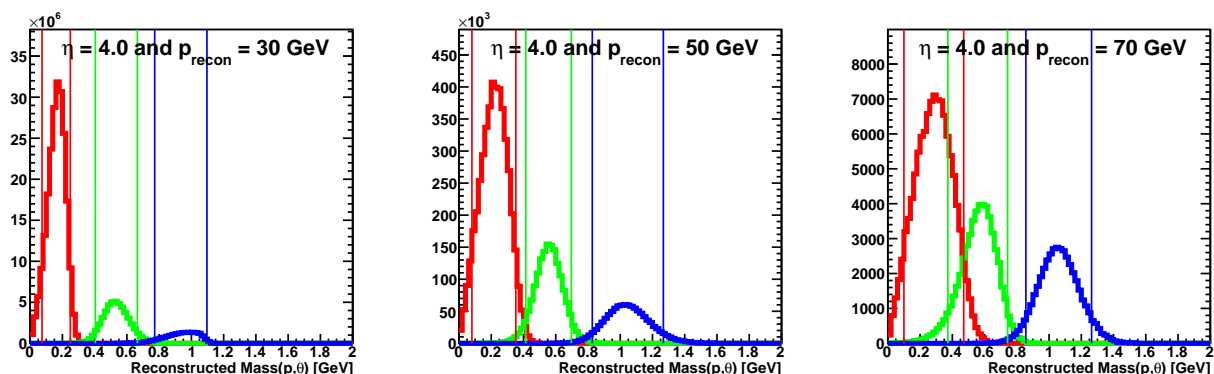
Figure 3.9: Reconstructed mass distribution via m(p,θ_{Crk}) at $\eta = 4$ for reconstructed momenta 30 GeV/c (left), 50 GeV/c (middle) and 70 GeV/c (right), for pions (red), kaons (green) and protons (blue), with the parent momentum and particle abundances from the PYTHIA generator. Vertical lines indicate the symmetric mass cuts corresponding to 90% efficiency. Note that particle true momentum is on the average smaller than reconstructed momentum, see Figure 3.10.

distance. One possibility for how this might be accomplished has been proposed by the Belle II experiment [27] and is shown in Figure 3.11. It uses several layers of aerogel with slightly different indices of refraction to achieve and approximate focusing of the light onto an image plane located behind the radiator. It should be possible to add additional layers of aerogel and optimize their thickness for producing the best quality ring for kaons using this technique, and therefore achieve good kaon-proton separation up to the highest momentum. One possibility for the photon detector would be large area Microchannel Plate detectors (MCPs), such as those being developed by the Large Area Picosecond Photodetector (LAPPD) Collaboration [16]. This effort is based on utilizing flat panel screen technology to produce large area MCPs at very low cost, while also preserving their excellent timing resolution (typically $\sim$ 20-30 ps). These devices would use multi-alkali photocathodes, which would be suitable for detecting the Cherenov light from aerogel with high efficiency, and also provide high gain for detecting single photoelectrons. The excellent time resolution would also provide additional time of flight capability when used in conjunction with the BBC to further enhance hadron particle ID. While this is still an R&D effort, it has already produced very encouraging results and has substantial support within the high energy physics community, and we feel that this would offer an attractive low cost, high performance readout for the aerogel detector.
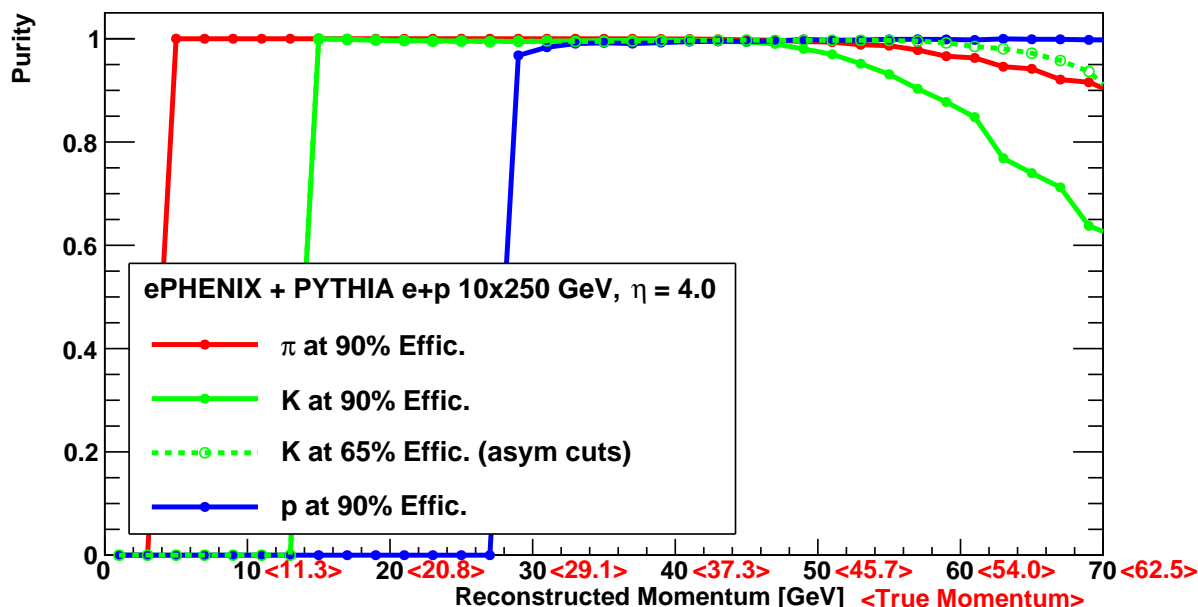
Figure 3.10: π, K, p purities at pseudorapidity 4.0 as a function of reconstructed momentum, based on symmetric cut on reconstructed mass corresponding to 90% efficiency (solid lines), and asymmetric cut with stricter selection on the kaons with efficiency 65% (dashed line); Also indicated in angle brackets are the values of the average true momentum at each reconstructed momentum, which are different due to momentum smearing and sharply falling momentum spectra.
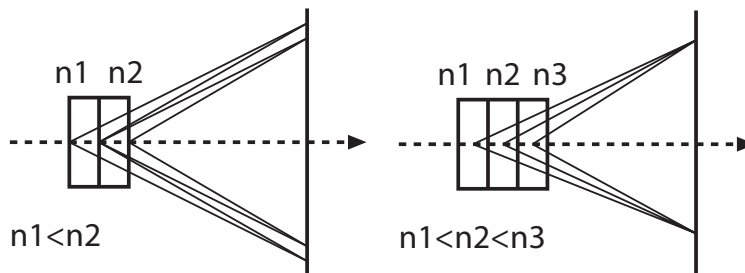
Figure 3.11: Approximate focusing method using two (left) and three (right) layers of aerogel with slightly different indicies of refraction proposed by Belle II [27]

3.5.3   DIRC

The main form of particle ID in the central region will be provided by a DIRC (Detection of Internally Reflected Čerenkov Light). The DIRC will be located at a radius of ~ 80 cm and extend ~ 8–10 cm in the radial direction. As we will be using the BaBar magnet for ePHENIX, it would be a major benefit to also acquire the BaBar DIRC, which was specifically designed to fit inside this magnet, and would completely satisfy the physics

(a) Nominal elevation view

(b) Cross section through the central tube
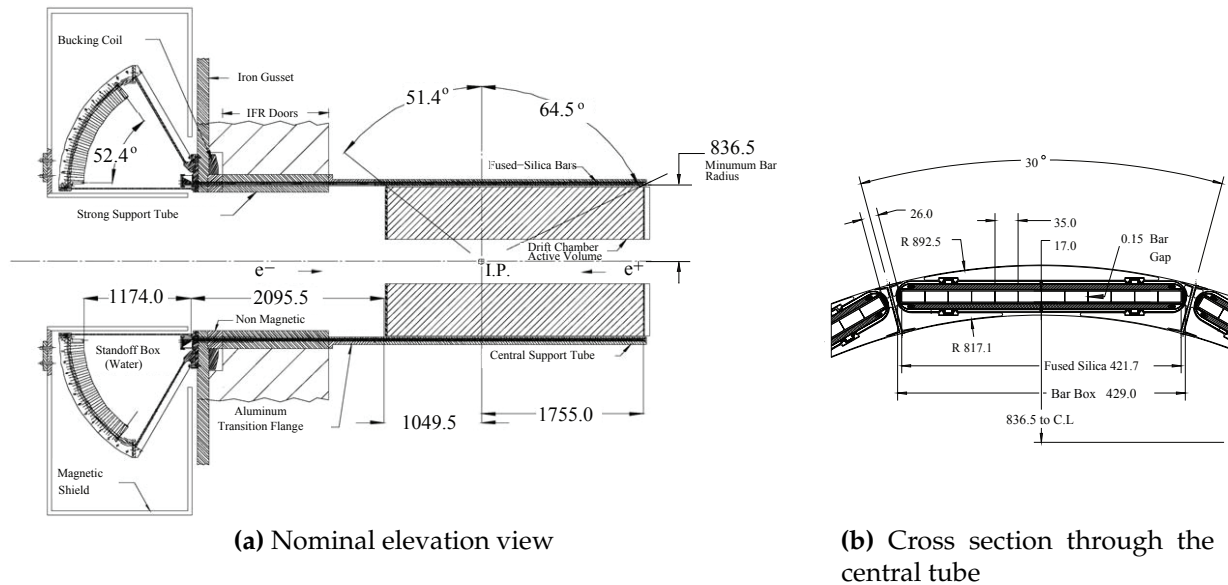
Figure 3.12: BaBar DIRC geometry [25]. All dimensions are given in mm.

requirements for ePHENIX. However, since it is not certain at this time that the BaBar DIRC will be available for ePHENIX, we consider it more as a model for the type of DIRC that would be required in terms of its construction and performance.

The BaBar DIRC, shown in Figure 3.12, consists of 144 precision fabricated quartz radiator bars that collect Čerenkov light produced by charged particles traversing the bars. In the BaBar DIRC, the quartz bars were read out on one end utilizing a large water filled expansion volume to allow the light to spread out and be read out using a large number (over 10,000) 28 mm diameter photomultiplier tubes.

The BaBar design, while allowing for a conventional PMT readout without the use of any focusing elements, requires a large expansion volume and this places stringent demands on the mechanical specifications for the detector. After the shutdown of BaBar at SLAC, it was proposed to use the DIRC in the SuperB Experiment in Italy. In doing so, it was also proposed to convert the original DIRC into a Focusing DIRC (FDIRC) [28], which would utilize mirrors at the end of the radiator bars, allowing for a considerable reduction in the size of the expansion region, more highly pixellated PMTs, and an overall expected improvement in performance. We would therefore propose the same modification of the BaBar DIRC for ePHENIX, or would construct a similar FDIRC if the BaBar DIRC were not available.

Similar to the BaBar technique [25], the hadron PID in the barrel will be analyzed using an event likelihood analysis with the DIRC and TPC dE/dx information simultaneously. A dE/dx measurement in the TPC gives very good hadron separation for very low momentum particles. But the ability of that technique to separate K-π and p-K drops off quickly around 0.5 GeV/c and 0.8 GeV/c, respectively. Meanwhile, the pions and kaons
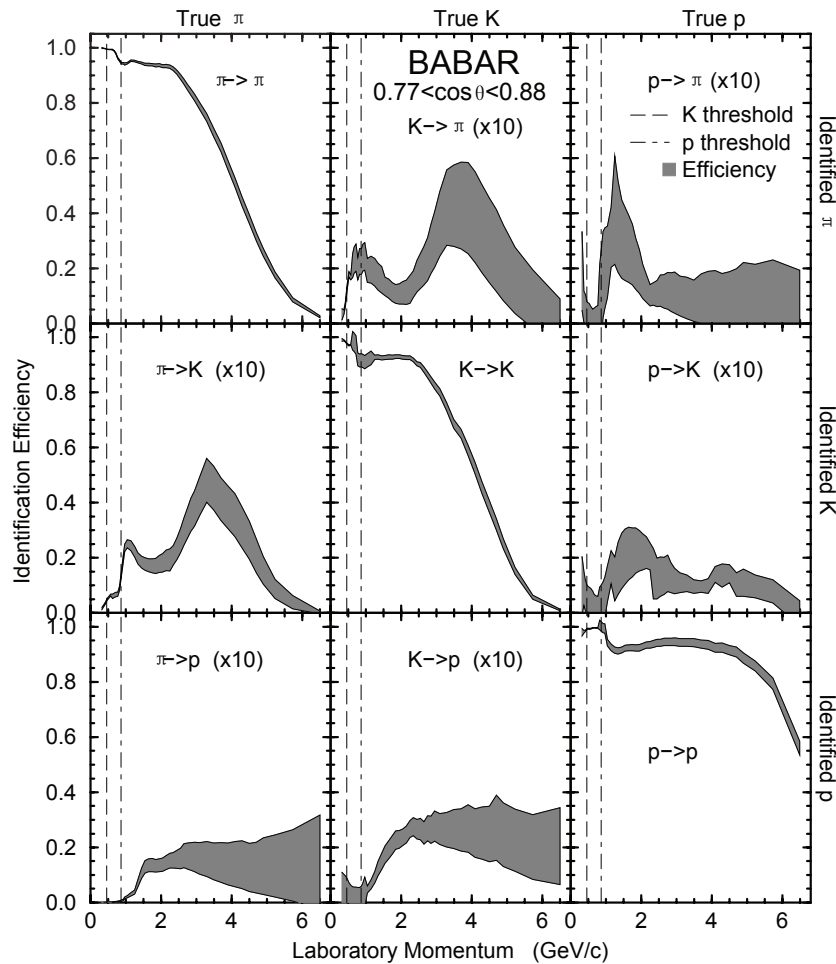
Figure 3.13: Simulated PID Efficiency matrix and its uncertainty for $1.0 < \eta < 1.4$ region, utilizing combined information of the BaBar DIRC and dE/dx measured in the tracking detector [25]. Note that the off-diagonal efficiency values are scaled by a factor of 10.

exceed their respective DIRC Čerenkov thresholds in this momentum region, as shown in Figure 3.6. Therefore, the DIRC sensitivity for K-π and p-K turns on sharply. A combined analysis of both pieces of information can give high PID purity up to a few GeV/c, as shown by the BaBar experiment [25]. At higher momenta, the DIRC ring resolution limits the separation capability. As shown in Figure 3.13, the K-π and p-K separation gradually drops below plateau above momentum of 2 and 5 GeV/c, respectively. A $\sim 20\%$ pion and kaon efficiency can still be maintained at 5 GeV/c. The vast majority of hadron kinematics in SIDIS can be covered in the 5×100 GeV/c collisions. In the 10×250 GeV/c collisions, the low to intermediate-z region in SIDIS are still well covered by this design.
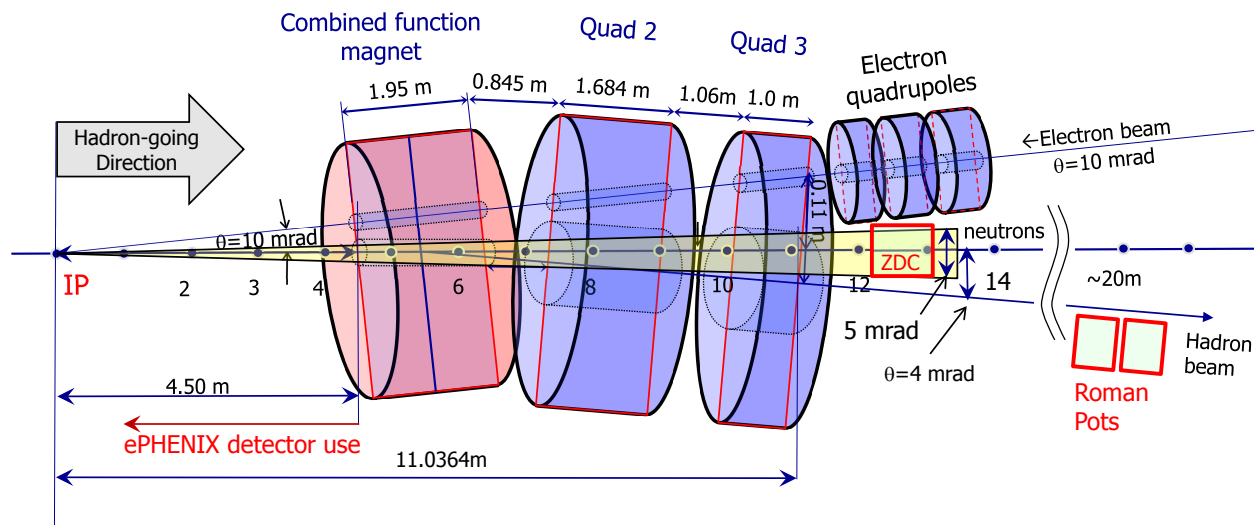
Figure 3.14: Floor plan show the locations for ZDC and Roman Pots relative to the ePHENIX interaction point. One layout of the interaction point magnets are also shown [29].

3.6   Beamline detectors

Two detectors will be installed near the outgoing hadron beam, downstream of the ePHENIX detector. They will be included in the eRHIC machine lattice design [3].

Zero Degree Calorimeter: A Zero Degree Calorimeter (ZDC) is planned for the hadron-going direction for the ePHENIX IP. Consistent with the eRHIC IR design (Figure 3.14), the ZDC will be installed about 12 meters downstream of the IP centered on the hadron direction at the IP. A 5 mrad cone opening of the IP is guaranteed by the ePHENIX detector and beam line magnets. The ZDC for the current PHENIX experiment [30] and its design can be reused for this device.

Roman Pots: In exclusive deep inelastic $e+p$ scattering, the final state proton will have a small scattering angle and escape the main ePHENIX detector. Two silicon tracking stations (also called the Roman Pot spectrometer) will be installed close to the beam, inside the beam pipe, downstream in the hadron-going direction to capture such protons. Each of the ePHENIX Roman Pot stations utilizes four tracking modules to cover the full azimuthal angles. Each of the tracking modules can use the design of the existing STAR Roman Pots [31]. Depending on the eRHIC lattice and magnet design, their location will be around 20 meters from the IP. This Roman Pot spectrometer will provide high efficiency for the exclusive DIS events in the $e+p$ collisions.

Chapter 4

Cost and Schedule

In this Chapter we detail a preliminary cost estimate for the ePHENIX detector. For each subsystem the cost basis is described and the totals for equipment, overhead, contingency and labor are summarized in table format. As previously described, ePHENIX is built on the foundation of the PHENIX experiment including the sPHENIX upgrade and fully utilizes the sPHENIX superconducting BaBar solenoid and barrel electromagnetic and hadronic calorimetry (whose costs are given in the sPHENIX MIE proposal). The costs for ePHENIX presented in Tables 4.1 and 4.2 here are totals, and there are significant opportunities for international and other non-DOE funding. In addition, we are actively pursuing other cost saving measures including the possible acquisition of the BaBar DIRC quartz, which is naturally well matched to the BaBar solenoid. The construction schedule for the ePHENIX detector spans a period of four years and would then be available for an eRHIC physics start in 2025.

4.1   Cost Assumptions and Methodology

As much as possible, costs are estimated from the costs of procurement of similar equipment by ourselves or other recent experiments of similar scale. We assume that the solenoid magnet and the barrel electromagnetic and hadronic calorimeters proposed for the sPHENIX detector will be the basis of the ePHENIX experiment. The cost estimate has been prepared as much as possible with the same assumptions used to estimate the cost of eRHIC, and therefore all costs are given in FY 2012 dollars without any inflation correction. Overhead rates have used the same assumptions used to estimate the cost of eRHIC adjusted for slightly different department organizational burdens. When estimating material costs that were given to us in Euros, an exchange rate of $1.25/€ has been used.

Labor costs are estimated from the mid-range physicists, engineers, and technicians which reflect Brookhaven direct costs and overheads, and a 3% yearly inflation rate. Brookhaven

rates are used for definiteness, but the actual labor costs may be expended at collaborating institutions which could differ.

4.2   Calorimetry

4.2.1   Endcap (electron-going) Crystal Electromagnetic Calorimeter

The cost of the Endcap Crystal Electromagnetic Calorimeter has been estimated using cost data provided by the PANDA experiment at FAIR, which has designed a similar endcap calorimeter. The higher light output form of lead tungstate (PWO-II) produced at the Shanghai Institute of Ceramics in China is, at the present time, the most economical choice of crystal for a high resolution calorimeter in a high rate environment. The cost estimate for $2.4 \times 2.4 \times 20$ cm^3 crystals for PANDA in quantities similar to those needed by ePHENIX is €600, or about €5/cm^3. The ePHENIX detector would require ~ 5000 crystals, which is slightly more than the PANDA endcap (4400). Cost estimates for the support structure and calibration system were also taken from the PANDA design.

4.2.2   Backward (hadron-going) Electromagnetic Calorimeter

The electromagnetic calorimeter in the hadron-going direction is assumed to be a lead-scintillating fiber design, similar to the tungsten-scintillating fiber central electromagnetic calorimeter for sPHENIX. The choice of lead versus tungsten was chosen to reduce the cost at an estimated price of $12/kg for processed lead, which is roughly 10% the cost of processed tungsten. The cost for the lead and scintillator for the backward EMCAL was then scaled using this number to the total volume.

4.2.3   Backward (hadron-going) Hadronic Calorimeter

The hadronic calorimeter in the hadron-going direction is assumed to be a steel-scintillating tile design read out with wavelength shifting fibers, similar to the sPHENIX central hadron calorimeter. The cost of the Backward HCAL was therefore obtained by scaling the cost of the sPHENIX central HCAL to the total volume of the Backward HCAL.

4.3   Tracking

4.3.1   Compact Time Projection Chamber

The cost of the TPC is based on other TPC's with a GEM readout that are currently being developed or designed, such as GEM TPC upgrade for ALICE [18], and the very large GEM TPC for the ILC [20, 21]. The ePHENIX TPC is rather small by comparison and requires a fast drift time. Such a fast, compact TPC with a radial extent from 20 to 70 cm and a length of ± 35 cm was studied several years ago as a possible upgrade to PHENIX, and is also similar to a TPC that was built for the LEGS experiment at Brookhaven. The ePHENIX TPC is somewhat longer, but the overall cost should be rather similar. The cost of the detector, gas system, and calibration system is based on the costs from the LEGS and STAR TPC projects, with a significant amount of engineering and design effort envisioned to realize a new design.

4.3.2   GEM Trackers

The cost of the forward and backward GEM trackers were estimated using the known costs of the large GEM tracking detectors being developed for the forward muon tracker for CMS. These are roughly 1 m long by 22–46 cm wide (tapered) triple GEM detectors that use foils produced at CERN using their new single sided etching technology. CERN is currently the only place capable of producing such large foils, but there are plans to transfer this technology to other manufacturing facilities (such as Tech Etch in Massachusetts which produced the GEM foils for the STAR Forward GEM Tracker). The cost of a single CMS detector is $\sim$ 5000 CHF, which includes the three GEM foils at 1200 CHF each, plus the mechanics of the detector. This works out to $\sim$ 15K CHF/m^2 for the whole detector. This factor was then scaled by the area and used for all of the forward and backward GEM trackers in ePHENIX.

4.3.3   Roman Pots

The cost of Roman Pots has been estimated using cost information from the STAR Roman Pots, detectors, and electronics. Labor costs have been calculated to include installation in the beam pipe.

4.4 Particle Identification

4.4.1 DIRC

Given that the BaBar magnet will be used for sPHENIX, it is natural to consider using the BaBar DIRC for particle identification in ePHENIX. The BaBar DIRC was recently intended to become a part of the SuperB detector. The plan was to convert it to a Focusing DIRC (FDIRC), which would eliminate the large expansion volume and improve its performance. The cost for doing this was estimated in detail for the SuperB project and is given in their TDR [32]. It was assumed that the quartz bars and boxes would be used as is, and that the additional cost would be to convert the optics to an FDIRC, replace the existing phototubes with new highly pixellated multi-anode PMTs, and ship all of the components to Italy. The cost of the contributed components from SLAC was equivalent to €5.8M and the cost for the new materials was €4.1M. We have assumed that the cost to acquire the BaBar DIRC and convert it to an FDIRC for sPHENIX is solely the latter, since it is already DOE property. This cost would then also conservatively include shipping the detector to BNL.

Since there are multiple requests for components of the BaBar DIRC system including for ePHENIX and there is ongoing study for the optimal radius for the ePHENIX inner barrel detectors, we have included in the costing the construction of an entirely new FDIRC using the same cost estimate as for SuperB. Acquiring the existing BaBar quartz radiators and support structures would result in a significant cost savings for the ePHENIX detector (∼$10M along with the associated labor and contingency that would be required to replicate those components that are included in Tables 4.1 and 4.2).

4.4.2 RICH and Aerogel

The RICH and aerogel detectors in ePHENIX are challenging due to their large area coverage and the requirement to measure rings for good particle identification. The gas RICH allows a technology that would use large area GEM detectors with CsI photocathodes to achieve the large area coverage with fine segmentation at a reasonable cost. This is similar to the technology used for the PHENIX Hadron Blind Detector (HBD), described in Ref. [33]. It would also utilize mirrors to focus the ring onto an image plane at the entrance of the detector. We estimate the cost of the detector based on the HBD to be ∼ $1M. The mirrors, gas system, and calibration system is estimated to cost an additional $1M.

The aerogel detector is a more challenging detector due to the fact that the Cherenkov light from the aerogel is in the visible wavelength range, and therefore the GEM-CsI technology could not be used as a large area photodetector. Other options do exist, such as Large Area Picosecond Photodetectors (LAPPDs), which would also provide excellent timing resolution, or SiPMs, which may become more cost effective for large area coverage on the time scale of ePHENIX. Since it is difficult to produce a cost estimate based on future technology, we have estimated the cost of the aerogel and its readout from the existing

PHENIX aerogel detector (which is only a threshold detector) scaled to the area of the ePHENIX aerogel. This gives a cost of $3.1M. While it is not clear at this time how the more highly segmented readout would be implemented, and would be an area for future R&D, the overall cost estimate for a detector of this type seems reasonable.

4.5   Electronics and Sensors

The cost for electronics and sensors is dominated by the channel count for the various detectors. We have tried to estimate the size of the readout elements for each detector (e.g., pads for the gas detectors and towers for the calorimeters) and scale by the area of each detector to estimate the channel count. We have then taken the cost per channel based on either known or estimated cost estimates for other similar detectors.

The crystal calorimeter would consist of $\sim$ 5000 crystals, and we assume each would be read out with 4 SiPMs in order to achieve good light collection efficiency and energy resolution. We further assume a cost of $20 per SiPM and a readout cost of $100/ch. For the Backward EMCAL, we assume towers corresponding to roughly $1R_M^2$, which leads to $\sim$ 26K towers, each read out with a single SiPM. For the Backward HCAL, we assume 10 $\times$ 10 cm^2 towers, giving $\sim$ 3000 towers, also read out with a single SiPM.

It is not clear what readout chips will be available for the TPC at the time they are needed for ePHENIX, but several TPCs currently under design are considering using the s-ALTRA chip for ALICE or the AFTER chip for PANDA. However, most of these cost estimates are not complete, so we have assumed the cost for the STAR TPC DAQ 1000 upgrade, which used the original ALTRA chip and had a cost of $16 per channel. We also assumed that the segmentation of the ePHENIX TPC readout planes would be $\sim$2 $\times$ 10 mm pads, which would lead to $\sim$ 180K pads, assuming both ends of the TPC are read out.

The segmentation of the GEM trackers was assumed to vary depending on their location. The inner most trackers were assumed to have 1 $\times$ 10 mm pads and the outer detectors were assumed to have 2 $\times$ 100 mm pads. This leads to $\sim$ 217K pads for the entire GEM tracking system. We assumed the readout cost to be similar to that of the CERN SRS readout system, which is $\sim$ €2.5/ch, although this would not necessarily be the actual readout system that is finally used.

The cost of the new readout for the FDIRC is included in the cost estimate for the new additional components given above. However, the readout electronics, as given in the SuperB TDR, is an additional €612K.

Based on recent developments by EIC R&D RICH group, we assume the segmentation of the gas RICH readout would correspond to roughly 0.25 cm^2 per pad with three readout channels per pad for charge sharing readout scheme, which is expected to enhance the ring resolution in RICH. This would lead to $\sim$ 220K channels. We further assume they would be read out with SRS type electronics at €2.5/ch, similar to the GEM trackers. For

the aerogel detector, we do not have an actual cost estimate for the readout, but we assume it will be included in the overall cost of $3.1M for the entire detector.

4.6   Equipment Cost

The costs of new equipment for each of the detectors in ePHENIX that are needed beyond the sPHENIX proposal are summarized in Table 4.1. As much as possible, the design relies on known technologies that do not require a large R&D effort to bring to operation, and builds on the experience of PHENIX operation and the sPHENIX design. The cost of electronics has been assessed separately from the detectors, and includes the sensors, in most cases silicon photomultipliers for the calorimetry, based on quotes for existing components.

4.7   Labor Cost

The cost of on-project labor for the nine detector projects and their associated electronics has been estimated from the cost of physicists, engineers, and technicians at Brookhaven in fully loaded at-year dollars assuming a four year construction schedule from FY2021–FY2025. Table 4.2 breaks down the rolled-up costs from the nine detector systems and their electronics by physicist, engineering, and technician effort. Sufficient effort is included in each project to account for management of the detector projects.

4.8   Schedule

The construction schedule is driven by the need to have the detector installed completely at the beginning of FY2025 for eRHIC and ePHENIX commissioning with four years of construction funding. The total project cost exceeds $20M, and so it will be managed in accordance with DOE Project Management Order 413.3B, and must obtain Critical Decisions. The complexity of the project suggests that a full Technical Design Report will require about two years to complete; in order for the project to begin significant construction funding in FY2021 beginning in October, 2020, CD2/3 approval would be needed no later than January, 2020, which would require a review in late 2019. CD1 approval would thus be needed in late 2017, which would allow for Preliminary Engineering Design (PED) funding to begin in FY2018. CD0 approval in late 2016 would allow a year to prepare the proposal for CD1 review. Table 4.3 summarizes the schedule of Critical Decisions envisioned.

Table 4.1: Estimated equipment costs for the ePHENIX detector (in $M).

		Cost	Overhead	Contingency	Total
Calorimeters	Endcap Crystal	3.40	0.47	1.93	5.80
	Forward EMCAL	1.41	0.27	0.84	2.53
	Forward HCAL	3.90	0.68	2.29	6.87
Tracking	TPC	0.75	0.19	0.47	1.41
	GEM Trackers	0.71	0.18	0.44	1.33
Beamline instrumentation	Roman pots	0.23	0.04	0.14	0.41
	Beam-Beam counter	0.20	0.05	0.13	0.38
Particle ID	DIRC	12.50	1.75	7.13	21.38
	RICH	2.00	0.50	1.25	3.75
	Aerogel	1.55	0.22	0.88	2.65
Electronics/sensors	Endcap Crystal	0.89	0.22	0.56	1.67
	Forward EMCAL	3.09	0.43	1.76	5.28
	Forward HCAL	0.38	0.05	0.22	0.65
	TPC	2.80	0.81	1.81	5.42
	GEM Trackers	0.71	0.18	0.44	1.33
	DIRC	0.77	0.19	0.48	1.44
	RICH	0.69	0.17	0.43	1.29
	Aerogel	1.55	0.39	0.97	2.91
	Roman Pots	0.11	0.03	0.07	0.21
	Beam-Beam	0.10	0.02	0.06	0.19
	Data Collection	0.60	0.15	0.38	1.13
	Trigger	0.60	0.15	0.38	1.13
Integration/Mechanical		3.00	0.93	1.96	5.90
Total		41.94	8.08	25.01	75.02

Table 4.2: Total estimated labor for ePHENIX detector construction.

	FY21	FY22	FY23	FY24	Total
Physicist FTE	10	9	10	13	42
Physicist cost	3.02	2.78	3.45	4.60	13.85
Engineer FTE	10	10	7	5	31
Engineer cost	2.59	2.66	2.02	1.49	8.76
Technician FTE	1	1	11	19	31
Technician cost	0.21	0.21	2.29	4.16	6.87
Total FTE	20	19	28	37	104
Total cost	5.81	5.65	7.77	10.25	29.49

Table 4.3: Schedule of Critical Decisions and reviews necessary for construction FY2021–FY2024.

CD0	4Q2016
CD1 review	4Q2017
TDR preparation	4Q2017 - 3Q2019
CD2/3 review	4Q2019
FY2021 budget briefing	1Q2020
Construction start	4Q2020 (FY2021)
CD4	3Q2024 (FY2024)
Commissioning run	1Q2025

Chapter 5

Collaboration Development and Manpower

As highlighted in this Letter of Intent, the PHENIX detector and the sPHENIX upgrade provide an excellent foundation for a new detector capable of addressing the exciting physics of the EIC. Similarly, the PHENIX collaboration provides an excellent foundation for a new collaboration able to carry out the required research and development, the detector design and construction, and the physics analysis for this EIC detector. We have used the name "ePHENIX" in this document as a placeholder for what we view as a new collaboration exploiting the physics potential of a new detector built around the BaBar magnet and barrel calorimetry of sPHENIX and utilizing the extensive infrastructure of the PHENIX intersection region.

The sPHENIX MIE proposal documents specific manpower needed for the design and construction of the magnet system and barrel calorimetry (see Chapter 6 of Ref. [1]). The calorimetry in the hadron-going direction of ePHENIX follows a similar design and would use a similar SiPM sensor and all digital electronic readout design. There is a natural application in ePHENIX of expertise being developed in these and other areas of technology. Members of the PHENIX collaboration are active on Generic Detector Research and Development for an Electron Ion Collider [34]. For instance, the RICH detector, which presents challenges in terms of light collection and readout within the active volume, is the target of an EIC R&D project led by Tom Hemmick (SUNY SB) with other members of PHENIX. There is also EIC R&D focused on tungsten-scintillator (or fiber) calorimetry with active participation from Craig Woody and Edouard Kistenev [35]. Another example is provided by Nevis laboratories, which has significant experience with all–digital readout electronics through the development of such a system for the PHENIX Hadron Blind Detector project, and these electronics are one option for the basis for the sPHENIX calorimetry readout. These would be similarly suitable for the additional new calorimetry for ePHENIX.

In most cases, these R&D intiatives are associated with larger consortia formed for the development of detector techologies for the EIC. These larger efforts already involve US and non-US institutions not directly involved in RHIC physics, but in JLab physics, and in some cases they involve institutions which are not currently involved in either RHIC or JLab physics, clearly indicating broader interest in the EIC in the US. We do expect that some of these groups would become involved in the ePHENIX detector collaboration in the coming decade.

Recently, a number of institutions have expressed strong interest in the heavy ion physics of sPHENIX and in the future ePHENIX. A successful ePHENIX project would require the addition of strong new institutions (particularly from the JLab user community in the US, but also the hadronic, DIS, and nuclear physics communities in Europe and Asia) in forming a new EIC collaboration. The current ePHENIX detector design concept attempts to limit the number of new technologies and custom electronics development projects, and yet, it has a number of key R&D projects that require additional expert groups. We see new groups playing a strong lead role in detector and design projects, as well as scientific leadership.

The PHENIX technicians and engineering support would most likely require augmentation during a full EIC detector construction phase, while at the same time they provide the core of an expert team for that evolution. The full cost of this labor is included in the the project cost detailed in Chapter 4.

Within the present PHENIX collaboration, the current physics focus is very rightly on the exciting spin and heavy ion physics underway and the sPHENIX upgrade physics. At the same time, there is growing excitement about an EIC program with the ePHENIX detector. This interest is both on the interesting detector development and the physics fronts. In fact, institutions that were very active in PHENIX early on and have now joined LHC experiments, are now actively engaging in the design for sPHENIX and ePHENIX. Overall, strong interest has been expressed by a number of PHENIX institutions in the physics and detector program of ePHENIX.

We expect that a collaboration of order ~ 500 active members (similar to PHENIX and STAR or H1 and ZEUS at HERA) will be required to design, build, and carry out the ambitious physics program. It is clear that some current PHENIX collaborators will move on to other projects on that time scale and that new institutions with both physics and detector expertise will join and participate — including in strong leadership roles. With guidance from Brookhaven National Laboratory management, we see a near future step involving a broad outside review of this Letter and the investment of time and effort in a set of workshops to get the earliest input on the various considerations for moving forward with ePHENIX.

Appendix A

ePHENIX LOI charge

Charge to PHENIX and STAR Collaborations: LOI for Transition to eRHIC

In 2010 the PHENIX and STAR collaborations each generated decadal plans laying out proposed science goals and detector upgrade paths for the period 2011-2020. At the request of ALD Vigdor, the Decadal Plan documents provided by both collaborations included conceptual ideas for utilizing these detectors for the study of ep and eA collisions in an early stage of the eRHIC program. In the case of PHENIX, the subsequent sPHENIX proposal includes a more extensive discussion of a possible ePHENIX upgrade through inclusion of additional particle identification and forward detectors.

We now have an EIC White Paper with a comprehensive outline of the physics questions for an Electron Ion Collider, a rapidly maturing machine design for eRHIC, and a clearer view of a possible path to an early-stage eRHIC program leading to first measurements in the mid-2020s. Therefore, the PHENIX and STAR Collaboration are now being asked to consider their role in a transition from RHIC to eRHIC on this time scale, and to provide specific plans (i.e. Letters of Intent) to upgrade/reconfigure the detectors from their present form to first-generation eRHIC detectors. These Letters of Intent (LOI) will be an important part of BNL's strategic planning as we move toward the next Nuclear Physics Long Range Plan. They should include an assessment of how the collaborations may evolve through this transition, and of the size and breadth of the scientific staffing required to carry out these plans.

In preparing these LOI the collaborations should assume an eRHIC machine with an electron beam energy up to 10 GeV, hadron beam energies as provided by the current RHIC machine (255 GeV for p and 100 GeV/nucleon for Au), and design luminosities of 10^{33} cm^{-2} s^{-1} for 10 GeV on 255 GeV ep collisions and the equivalent of 6×10^{32} cm^{-2} s^{-1} for 10 GeV on 100 GeV/ nucleon eA collisions.

The LOI should include a description of the physics reach of the upgraded detectors, based on their detection capabilities, taking into consideration the key measurements identified in the EIC White Paper for Stage 1 (but now for 10 GeV electrons instead of 5 GeV). Further

details of the desired detector requirements will be soon posted by the eRHIC Task Force on a Wiki page.

The technical details of the proposed upgrades should be given in sufficient detail to make a preliminary cost estimate. We assume that the upgrades may come in stages, with some elements implemented during the on-going RHIC heavy ion operations. Sufficient detail should be provided for each step to allow a rough outline of the overall construction schedule, assuming a 2–3 year shut-down of collider operations before the commencement of eRHIC operations, and an estimate of the required funding profile.

The Letters of Intent should be submitted by September 30, 2013. A brief statement of progress by each collaboration at the time of the June 2013 PAC meeting would be appreciated.

Bibliography

[1] C. Aidala et al. sPHENIX: An Upgrade Concept from the PHENIX Collaboration. 2012. `arXiv:1207.6378`. (document), 3, 5

[2] PHENIX Collaboration. The PHENIX Decadal Plan, 2010. URL: `http://www.phenix.bnl.gov/phenix/WWW/docs/decadal/2010/phenix_decadal10_full_refs.pdf`. (document)

[3] A. Accardi et al. Electron Ion Collider: The Next QCD Frontier - Understanding the glue that binds us all. 2012. `arXiv:1212.1701`. (document), 1, 1.1, 1.2, 1.3, 1.3.1, 1.3, 1.3.2, 1.6, 2, 3.6

[4] 2007 Long Range Plan: The Frontiers of Nuclear Science, 2007. URL: `http://science.energy.gov/~/media/np/nsac/pdf/docs/NuclearScienceHighRes.pdf`. 1

[5] D. de Florian, R. Sassot, M. Stratmann, and W. Vogelsang. Extraction of Spin-Dependent Parton Densities and Their Uncertainties. *Phys. Rev.*, **D**80:034030, 2009. `arXiv:0904.3821, doi:10.1103/PhysRevD.80.034030`. 1.2

[6] M. Anselmino et al. Transversity and Collins functions from SIDIS and e^+e^- data. *Phys. Rev.*, **D**75:054032, 2007. `arXiv:hep-ph/0701006, doi:10.1103/PhysRevD.75.054032`. 1.3.1

[7] X.-D. Ji. Gauge invariant decomposition of nucleon spin and its spin - off. *Phys. Rev. Lett.*, 78:610–613, 1997. `arXiv:hep-ph/9603249, doi:10.1103/PhysRevLett.78.610`. 1.3.1

[8] A. Airapetian et al. Hadronization in semi-inclusive deep-inelastic scattering on nuclei. *Nucl. Phys.*, B780:1–27, 2007. `arXiv:0704.3270, doi:10.1016/j.nuclphysb.2007.06.004`. 1.3.2, 1.4

[9] D. Boer et al. Gluons and the quark sea at high energies: Distributions, polarization, tomography. 2011. `arXiv:1108.1713`. 1.3.2, 2

[10] A. Daniel et al. Measurement of the nuclear multiplicity ratio for K_s^0 hadronization at CLAS. *Phys. Lett.*, B706:26–31, 2011. `arXiv:1111.2573, doi:10.1016/j.physletb.2011.10.071`. 1.4

[11] E. Iancu, K. Itakura, and L. McLerran. Geometric scaling above the saturation scale. *Nucl. Phys.*, A708:327–352, 2002. `arXiv:hep-ph/0203137, doi:10.1016/S0375-9474(02)01010-2`. 1.5

[12] F. Sauli. GEM: A new concept for electron amplification in gas detectors. *Nucl. Instrum. Meth.*, A386:531–534, 1997. `doi:10.1016/S0168-9002(96)01172-2`. 3

[13] P. Abbon et al. The COMPASS experiment at CERN. *Nucl. Instrum. Meth.*, A577:455–518, 2007. `arXiv:hep-ex/0703049, doi:10.1016/j.nima.2007.03.026`. 3

[14] R. Bell et al. The BaBar superconducting coil: Design, construction and test. *Nucl. Phys. Proc. Suppl.*, 78:559–564, 1999. `doi:10.1016/S0920-5632(99)00603-9`. 3.1

[15] S. An et al. A 20-ps timing device: A Multigap Resistive Plate Chamber with 24 gas gaps. *Nucl. Instrum. Meth.*, A594:39–43, 2008. `doi:10.1016/j.nima.2008.06.013`. 3.2.1

[16] B. Adams et al. Measurements of the Gain, Time Resolution, and Spatial Resolution of a 20x20cm MCP-based Picosecond Photo-Detector. *Proceedings of the Vienna Conference on Instrumentation*, 2013. URL: `http://psec.uchicago.edu/library/doclib/documents/222/sendit`. 3.2.1, 3.5.2

[17] B. Yu et al. A gem based tpc for the legs experiment. In *Nuclear Science Symposium Conference Record, 2005 IEEE*, volume 2, pages 924–928, 2005. `doi:10.1109/NSSMIC.2005.1596405`. 3.2.2

[18] L. Musa et al. Letter of intent for the upgrade of the alice experiment. Technical Report LHCC-I-022, CERN, 2012. 3.2.2, 4.3.1

[19] B. Ketzer. A Time Projection Chamber for High-Rate Experiments: Towards an Upgrade of the ALICE TPC. 2013. `arXiv:1303.6694`. 3.2.2

[20] T. Abe et al. The International Large Detector: Letter of Intent. 2010. `arXiv:1006.3396`. 3.2.2, 4.3.1

[21] P. Schade and J. Kaminski. A large TPC prototype for a linear collider detector. *Nucl. Instrum. Meth.*, A628:128–132, 2011. `doi:10.1016/j.nima.2010.06.300`. 3.2.2, 4.3.1

[22] C. Woody. Future Applications of GEM Detectors at BNL. Technical report, 2013. Talk on RD51 Collaboration Meeting. 3.2.3, 3.2.4

[23] D. Abbaneo et al. Technical Proposal A GEM Detector System for an Upgrade of the CMS Muon Endcaps. Technical report, 2012. 3.2.3

[24] Technical Design Report for PANDA Electromagnetic Calorimeter (EMC). 2008. `arXiv:0810.1216`. 3.3.1, 3.5

[25] I. Adam et al. The DIRC particle identification system for the BaBar experiment. *Nucl. Instrum. Meth.*, A538:281–357, 2005. `doi:10.1016/j.nima.2004.08.129`. 3.6b, 3.5, 3.12, 3.5.3, 3.13

[26] W. Anderson et al. Design, Construction, Operation and Performance of a Hadron Blind Detector for the PHENIX Experiment. *Nucl. Instrum. Meth.*, A646:35–58, 2011. `arXiv:1103.4277, doi:10.1016/j.nima.2011.04.015`. 3.5.1

[27] T. Iijima et al. A Novel type of proximity focusing RICH counter with multiple refractive index aerogel radiator. *Nucl. Instrum. Meth.*, A548:383–390, 2005. `arXiv:physics/0504220, doi:10.1016/j.nima.2005.05.030`. 3.5.2, 3.11

[28] E. Grauges et al. SuperB Progress Reports – Detector. 2010. `arXiv:1007.4241`. 3.5.3

[29] D. Trbojevic, 2013. Private communication. 3.14

[30] C. Adler et al. The RHIC zero degree calorimeter. *Nucl. Instrum. Meth.*, A470:488–499, 2001. `arXiv:nucl-ex/0008005, doi:10.1016/S0168-9002(01)00627-1`. 3.6

[31] L. Adamczyk et al. Single Spin Asymmetry A_N in Polarized Proton-Proton Elastic Scattering at $\sqrt{s} = 200$ GeV. *Phys. Lett.*, B719:62–69, 2013. `arXiv:1206.1928, doi:10.1016/j.physletb.2013.01.014`. 3.6

[32] SuperB Collaboration, E. Grauges, F. Forti, B. N. Ratcliff, and D. Aston. SuperB Progress Reports – Detector. *ArXiv e-prints*, July 2010. `arXiv:1007.4241`. 4.4.1

[33] W. Anderson et al. Design, construction, operation and performance of a Hadron Blind Detector for the PHENIX experiment. *Nucl. Instrum. Meth.*, A646(1):35 – 58, 2011. URL: `http://www.sciencedirect.com/science/article/pii/S0168900211007534`, `doi:http://dx.doi.org/10.1016/j.nima.2011.04.015`. 4.4.2

[34] Generic Detector Research and Development for an Electron Ion Collider. URL: `http://wiki.bnl.gov/conferences/index.php/EIC_R%25D`. 5

[35] H. Huang et al. Status Report and Proposal for EIC Calorimeter Development, 2013. URL: `https://wiki.bnl.gov/conferences/images/3/30/RD-1_EIC_CAL-Consortium-May2013.pdf`. 5